






Article

Seeding as a Decisive Tool for Increasing Space-Time-Yields in the Preparation of High-Quality Cu/ZnO/ZrO₂ Catalysts

David Guse ¹, Lucas Warmuth ², Moritz Herfet ², Katharina Adolf ¹, Thomas A. Zevaco ², Stephan Pitter ²
and Matthias Kind ^{1,*}

¹ Karlsruhe Institute of Technology, Institute of Thermal Process Engineering, Kaiserstr. 12, 76131 Karlsruhe, Germany; david.guse@kit.edu (D.G.)

² Karlsruhe Institute of Technology, Institute of Catalysis Research and Technology, Hermann-von-Helmholtz-Platz 1, 76344 Eggenstein-Leopoldshafen, Germany; stephan.pitter@kit.edu (S.P.)

* Correspondence: matthias.kind@kit.edu

Abstract: Aging is one of the key steps in the preparation of highly active Cu/ZnO-based catalysts for use in the production of methanol. If certain pH and temperature specifications are met, an initially amorphous precipitate transforms into the crystalline precursor phase of zincian malachite, which is characterized by a periodic arrangement of Cu and Zn atoms and has proven advantageous for the quality of the final catalyst. However, aging generally takes between 30 min and multiple hours until the desired phase transformation is completed. With our study, we show that aging can be significantly accelerated by seeding the freshly precipitated suspension with already aged zincian malachite crystals: the necessary aging time was reduced by 41% for seeding mass fractions as low as 3 wt.% and from 83 min to less than 2 min for 30 wt.% seeds. No negative influence of seeding on the phase composition, specific surface area, molar metal ratios, or the morphology of the aged precursor could be identified. Consequently, the catalyst performance in the synthesis of methanol from CO₂, as well as from a CO/CO₂ mixture, was identical to a catalyst from an unseeded preparation and showed small advantages compared to a commercial sample. Thus, we conclude that seeding is a vital tool to accelerate the preparation of all Cu/Zn-based catalysts while maintaining product quality, presumably also on an industrial scale.

Keywords: aging; catalyst preparation; continuous co-precipitation; copper-zinc catalyst; seeding; space-time-yield



Citation: Guse, D.; Warmuth, L.; Herfet, M.; Adolf, K.; Zevaco, T.A.; Pitter, S.; Kind, M. Seeding as a Decisive Tool for Increasing Space-Time-Yields in the Preparation of High-Quality Cu/ZnO/ZrO₂ Catalysts. *Catalysts* **2024**, *14*, 517. <https://doi.org/10.3390/catal14080517>

Academic Editor: Zhixin Yu

Received: 21 July 2024

Revised: 2 August 2024

Accepted: 6 August 2024

Published: 9 August 2024



Copyright: © 2024 by the authors. Licensee MDPI, Basel, Switzerland. This article is an open access article distributed under the terms and conditions of the Creative Commons Attribution (CC BY) license (<https://creativecommons.org/licenses/by/4.0/>).

1. Introduction

The chemical industry faces a dilemma. On the one hand, there are efforts to become sustainable and as CO₂-neutral as possible in the future. Yet, on the other hand, the demand for commodity chemicals from non-renewable resources is still increasing; for instance, the annual production of methanol is expected to increase from the current level of approx. 100 Mt to 500 Mt in 2050 [1,2]. Currently, more than 99% of methanol is produced from syngas, that has been synthesized by steam reforming or coal gasification, in a low-pressure catalysis, mostly using Cu/ZnO/Al₂O₃ catalysts [1,3–6].

A possible solution in this case is the production of green methanol from H₂, which is produced by electrolysis powered by wind or solar energy, and CO₂ drawn from industrial point sources [7–11]. However, by substituting CO with CO₂, water is formed as a by-product of catalysis, which poisons and deactivates the Cu/ZnO/Al₂O₃ catalyst [5,7,12,13]. Thus, alternative catalyst compositions are necessary for the synthesis of methanol from CO₂. Recent studies prove that applying ZrO₂ as a promoter instead of Al₂O₃ is a very promising approach [7,14–17]. However, one major challenge remains: due to the formation of water by the reverse water-gas shift reaction, the productivity over the time-on-stream decreases [15] and the lifetime of the catalyst is shortened significantly by reversible [18]

and irreversible [19] deactivation. Therefore, the catalyst has to be replaced regularly. Thus, in addition to further optimization of the catalyst itself, future research should also focus on how the catalyst manufacturing process can be scaled up while maintaining a consistent product quality and how its efficiency, which is quantifiable as the space-time yield, can be optimized.

Catalyst Preparation

In general, the most important catalyst properties to ensure high methanol productivity [20–22], selectivity [23] and lifetime [24] are the specific surface area, the copper surface area, and the periodic and finely distributed arrangement of Cu and Zn atoms, as well as their contact and the pore characteristics of the catalyst. Manifold studies showed that by forming the mineral phase zincian malachite as a precursor during the preparation of the catalyst, all of these properties, and, thus, the catalyst's performance in methanol synthesis, are improved [21,22,25–27]. This is caused by the periodic arrangement of Cu and Zn atoms in the crystal lattice of said phase ($[\text{Cu}_{1-\tilde{x}_{\text{Zn,zm}}}\text{Zn}_{\tilde{x}_{\text{Zn,zm}}}]_2(\text{CO}_3)(\text{OH})_2$) [28]. Particularly advantageous are Zn fractions that are as close to the thermodynamically limited maximum values ($\tilde{x}_{\text{Zn,zm}} \leq 0.27$ mol% [29] or $\tilde{x}_{\text{Zn,zm}} \leq 0.31$ mol% [30]) as possible [30,31]. Additionally, the needle-like morphology of the initial crystals, which aggregate to spherical entities, results in large surface areas and beneficial pore sizes [21,22,25,27]. Rosasite is a naturally occurring variation, with Zn fractions of up to approx. 42 mol% and very similar space group symmetry operators, and it is often applied as a reference phase for XRD and IR analysis [29,32].

However, due to kinetic restraints, zincian malachite cannot be precipitated directly from the reactant solutions [30,33,34]. Instead, an often amorphous precursor forms first by co-precipitation when a metal nitrate solution is mixed with an alkaline Na_2CO_3 or NaHCO_3 solution [34–36]. In a previous study, we found that Cu and Zn can be inhomogeneously distributed in this amorphous material if mixing is too slow and/or local pH peaks are present during precipitation. Furthermore, the amorphous precursor shows a spherical morphology with a low surface area [35]. Thus, if the subsequent aging step is skipped, this material results in a catalyst with comparatively low productivity [27,37].

However, if an aging step follows, the amorphous precursor transforms into zincian malachite, possibly by the incorporation of Zn^{2+} ions from the solution, when a temperature between typically 60 °C and 70 °C and $6 \leq \text{pH} \leq 7$ in the mother liquor are maintained [26,31,32,38]. Zn fractions above approx. 30 mol% are to be avoided, due to the formation of the by-products aurichalcite ($[\text{Zn}, \text{Cu}]_5(\text{CO}_3)_2(\text{OH})_6$) and hydrozincite ($\text{Zn}_5(\text{CO}_3)_2(\text{OH})_6$). These are rich in Zn, which affects the catalyst performance negatively [31]. Similarly, if the pH is too high, CuO forms instead, resulting, again, in the separation of Cu and Zn atoms [39]. When $\text{pH} < 6$, gerhardtite forms, resulting in the unfavorable incorporation of NO_3^- anions into the material [39]. Deviating from the optimum temperature and pH range also leads to decreased BET surface areas and catalyst productivity [20,40]. Thus, to obtain a high-quality catalyst, it is essential to meet the specifications and obtain zincian malachite as the main aging product [26,31].

While the formation of initial solids by co-precipitation is completed in milliseconds to seconds [35,41,42], aging takes, in general, at least 30 min and up to several hours [43–46] until the phase transformation is completed. Gldenpfennig et al. conducted milliliter-scale tests and found that the phase transformation comprises a long induction period until, first, zincian malachite particles are present, followed by a brief transformation time until recrystallization is completed [47]. This phase transformation is accompanied by a distinct pH minimum [26,36,48–50]. Thus, pH can be used, along with a change in the suspension color from blue to green [48,49], to analyze when the phase change from (zincian) georgeite to zincian malachite occurs. Other methods, such as XRD or FT-IR analysis, confirm the necessary aging times determined by pH and color [36,48].

After the phase change of the precursor material is completed, the aged particles are filtered, washed to eliminate any residues of Na^+ and NO_3^- , which are detrimental to the catalyst performance and lifetime [36,51,52], and dried [26,53]. During the subsequent

calcination, the aged precursor decomposes into CuO and ZnO, as well as ZrO₂ and/or Al₂O₃, to form the precatalyst while maintaining specific pore characteristics and a beneficial arrangement of Cu and Zn atoms on the nanoscale [27]. Finally, the material is shaped and CuO is reduced to Cu [26,54] to obtain a catalytically active material with the advantageous surface area, nano-homogeneity and nano-dispersity that result from the intermediate phase, zincian malachite.

In summary, aging is one of the key steps in determining the quality of the final catalyst material. It is also a process step with high economic savings potential, due to the long process time and the large amount of water used as a solvent. Thus, in order to increase the space-time yield of the preparation, the aim must be to reduce the aging time without affecting the product quality negatively. This further increase of the solids concentration during aging is an alternative approach to increase space-time yield. However, it is, in general, limited by the solubility of the reactant solutions.

Aging Kinetics

There are some studies in the literature that focus on how to decrease the necessary aging time to complete the phase transformation. Guldenpfennig et al. demonstrated that the metal ratio, temperature and pH each influence aging kinetics [47]. However, these parameters cannot be chosen arbitrarily because they also influence the physicochemical properties of the intermediate stage and, thus, the catalyst properties. We previously demonstrated that increasing the energy dissipation rates during the mixing of the two reactant solutions can nearly quadruple the specific surface area of the initial co-precipitate. Higher mass-specific surface areas greatly improved aging kinetics [35]. However, seeding with the aimed-at crystalline phase appears to be the most promising approach to improve aging kinetics and, thereby, reduce aging times [46,47].

Seeding is commonly used in industrial crystallization to improve process control and reproducibility, particularly when small particles are involved or when the process is carried out within the metastable zone limit of primary nucleation [55,56]. This allows for secondary nucleation instead of uncontrolled primary nucleation, as well as control over polymorphism [57–60]. In general, a seeding weight fraction x_{Seeds} of 0.1 to 1.0 wt.% according to Equation (1) is required to allow secondary nucleation below the metastable zone limit [61]. Seeding is also used to obtain defined particle shapes and size distributions, which affect the filterability and flow properties of the particles in downstream processes. This may also be crucial for the contemplated application, e.g., due to the resulting dissolution properties of proteins [57] or the surface and microstructure properties of the catalyst [35,62,63].

$$x_{\text{Seeds}} = \frac{m_{\text{Seeds}}}{m_{\text{solids,total}}} \quad (1)$$

Guldenpfennig et al. reduced the necessary induction time for a binary Cu/Zn-based system by up to 47% by adding a small volume of aged suspension containing zincian malachite to the reaction vessel before mixing ($x_{\text{Seeds}} = 0.04$). The higher the seed fraction, the shorter the induction time appeared to be. However, these findings are limited to small volumes on the milliliter scale and a total metal nitrate concentration in the suspension of $\tilde{c}_{\text{M,susp}} = 0.1 \text{ M}$ [47], cf. Equation (2).

$$c_{\text{M,susp}} = \frac{n_{\text{Cu(NO}_3)_2} + n_{\text{Zn(NO}_3)_2} + n_{\text{ZrO(NO}_3)_2}}{V_{\text{susp}}} \quad (2)$$

Guse et al. confirmed these results at the liter scale and $\tilde{c}_{\text{M,susp}} = 0.14 \text{ M}$ for a Cu/ZnO/ZrO₂ precursor at two different pH_0 , where aging times were reduced by up to 50% for $x_{\text{Seeds}} = 0.03$ and from 96 min to 8 min for $x_{\text{Seeds}} = 0.42$. Furthermore, an analysis of the phase composition after aging, as well as the metallic composition, mass-specific surface area, the mean pore size and the morphology of the precatalyst after calcination, indicated that seeding does not influence the properties of the material negatively, despite

the vastly reduced aging time [46]. Only the FT-IR results indicated that aurichalcite may accumulate with repeated seeding, which could not be confirmed by XRD evaluation.

Objectives

Based on the results by Gldenpfennig et al. [47] and Guse et al. [46], we seek to validate if the reduction of aging time by seeding can be confirmed for industrially relevant solids concentrations of more than 5 wt.% to optimize the space-time yield. Furthermore, the impact of the seeding method and how the reduction of aging times correlates with the mass fraction and surface area of seeds is investigated. Ultimately, our goal is to clarify if the vastly reduced aging time does affect the catalyst's properties and, thus, its performance in methanol synthesis. We believe that the product quality should be unaffected if the phase change to zincian malachite is completed. On this basis, a recommendation on how to conduct seeded aging for a maximum space-time yield without compromising product quality will be given.

2. Results and Discussion

First, we discuss the influence of seeding (cf. Section 3.2) on aging kinetics and the resulting aging time and space-time yield. The influences of the seed mass fraction, the seeding method and the particle size of the seeds on the aging kinetics will be analyzed in detail. Then, for the chosen parameters, the influence of seeding on the resulting physicochemical properties of the aged precursors as well as those of the precatalyst will be thoroughly investigated. Finally, the impact on the catalyst's performance in terms of methanol synthesis is evaluated.

2.1. Influence of Seeding on Aging Kinetics and Space-Time-Yield

2.1.1. Seed Mass Fraction

As a reference, the pH profile as a function of the aging time is plotted in Figure 1a for seven independent unseeded Cu/ZnO/ZrO₂ preparations, with $b_{M,susp} = 0.14 \text{ mol} \cdot \text{kg}_{\text{H}_2\text{O}}^{-1}$ at $T = 55 \text{ }^\circ\text{C}$. This corresponds to a solids weight fraction of approx. 2 wt.% in the suspension. In Figure 1b, the same aging conditions were applied but a varying amount of freshly prepared seeds were added directly after co-precipitation was completed (cf. Section 3.2).

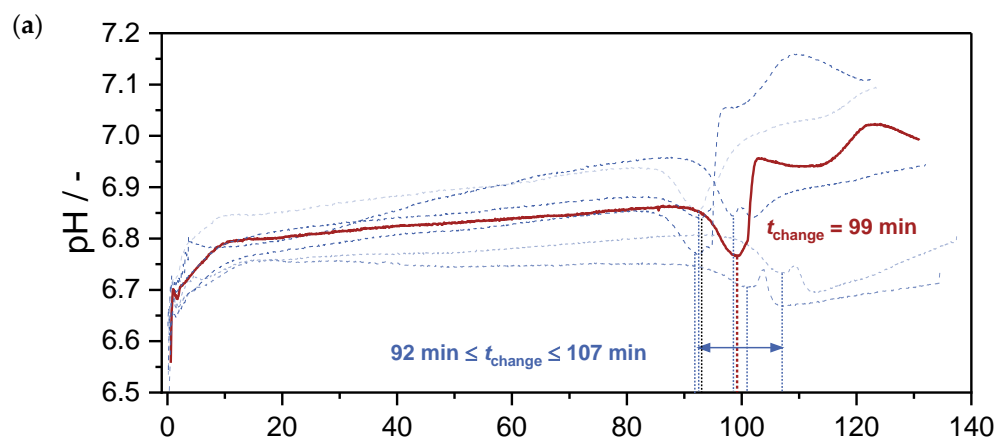


Figure 1. Cont.

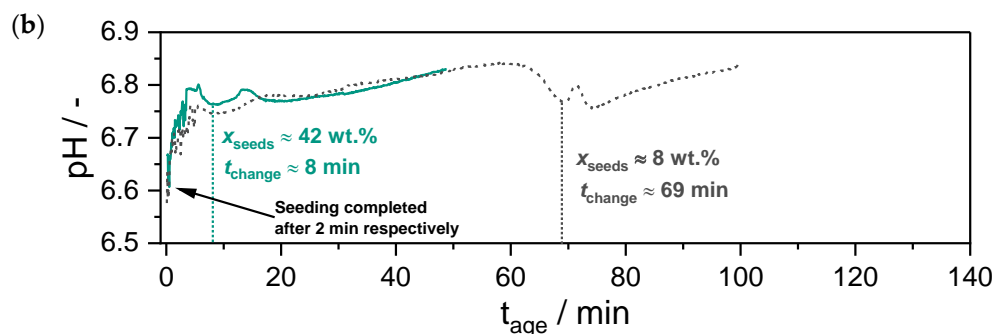


Figure 1. Evolution of pH as a function of the aging time t_{age} from Guse et al. [46]: (a) seven independent unseeded reference experiments; (b) two seeded experiments with $x_{Seeds} = 8$ wt.% and $x_{Seeds} = 42$ wt.%, respectively.

The curves in Figure 1a all show the same characteristics and, thus, the reproducibility of the preparation and the necessary aging time when the same process conditions are applied. First, during the wetting of the pH electrode, the pH rises sharply up to the intended start value of $pH(t_{age} = 0 \text{ min}) = 6.7$. From here on, the pH is almost stable and rises, if at all, only slightly. After a total aging time of 92 to 107 min, a pH minimum is passed that coincides with a change in color [46] and indicates that the phase change to zincian malachite is completed [26,44,64]. This is confirmed by the XRD evaluation shown in Figure 2a and the FT-IR evaluation in the Supplementary Materials. Aging is continued for an additional 30 min after the pH minimum is reached, to ensure that the phase change is completed for each particle. In some cases, a second pH minimum occurred 5–10 min after the first. However, it could not be correlated to any events; it did not affect the FT-IR spectrum or the X-ray diffractogram (cf. Figures S1 and 2) and is unknown in the literature. Temporary deposits on the probe during the phase transformation might be a possible cause. The three stages of rapid pH increase, slow pH increase and pH minimum are also present for both seeded experiments in Figure 1b. Yet, depending on the seed mass fraction chosen, the pH minimum that corresponds to the phase transformation already occurs after $t_{change} = 69$ min for $x_{Seeds} = 8$ wt.% and, respectively, after only 8 min of aging for $x_{Seeds} = 42$ wt.%. Again, the phase transformation is confirmed by the XRD analysis in Figure 2b and the FT-IR analysis in the Supplementary Materials.

Figure 2 shows the evolution of the X-ray diffractogram as a function of aging time for an exemplary unseeded aging process and for $x_{Seeds} = 10$ wt.%, where, respectively, samples were taken approx. every 20 min. When no seeding is applied ($x_{Seeds} = 0$ wt.%) all four samples for $t_{age} \leq 60$ min exhibit an amorphous diffractogram. Simultaneously, the XRF evaluations in Figure 3a show a consistent Zn fraction in the solids throughout the aging process, with no discernible trend. This implies that both Cu and Zn co-precipitate directly ($t_{age} \rightarrow 0$ min) and that no subsequent incorporation of Zn ions from the solution occurs. Instead, a single amorphous Cu/Zn precursor phase (zincian georgeite) or, less probably, several amorphous precursor phases must form in the early stages of aging, which is compatible with the findings reported in the literature [34,48,65]. The first crystalline structures appear in the 80-min sample, indicating the beginning of the transformation from zincian georgeite to zincian malachite [27,36]. However, the evaluation of $\tilde{x}_{Zn,zm}$ in Figure 3a indicates substantial uncertainty up to 100 min, showing that a change in crystal structure is ongoing and that a high fraction of amorphous solids is still present. After the phase shift, which is indicated by the pH minimum in Figure 1a and a color change, consistently high Zn fractions in the predicted range of $\tilde{x}_{Zn,zm} \approx 0.27$ are prevalent in Figure 3a. In general, the total Zn fractions obtained from ICP-OES and XRF are between $\tilde{x}_{Zn,metals} = 0.277$ and $\tilde{x}_{Zn,metals} = 0.321$, which corresponds to the expected value of $\tilde{x}_{Zn,metals} = 0.3$. The Rietveld refinement (cf. Section 2.2.1) verified the presence of minor amounts of Zn-rich aurichalcite or hydrozincite ($0.3 \text{ wt.}\% < x_{aur} < 6.4 \text{ wt.}\%$) in addition to zincian malachite at $\tilde{x}_{Zn,zm} \approx 0.27$.

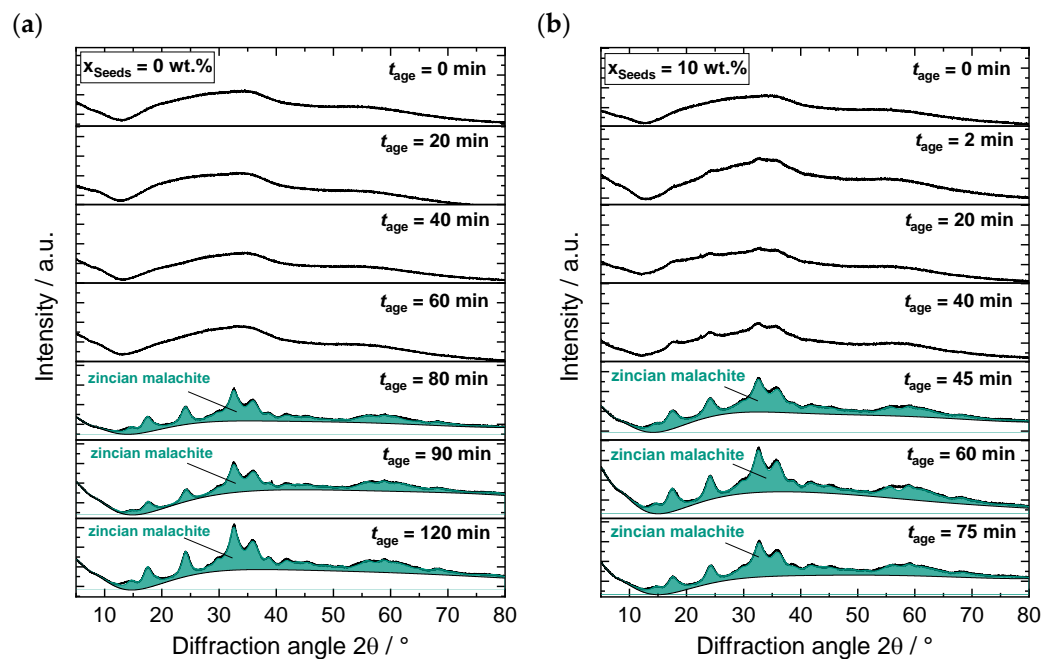


Figure 2. X-ray diffractograms of dried and washed samples as a function of aging time for: (a) the standard aging process without seeding ($x_{Seeds} = 0$ wt.%) and (b) a preparation where seeds were added after co-precipitation was completed at $t_{age} = 0$ min ($x_{Seeds} = 10$ wt.%). The phase composition was evaluated by Rietveld refinement.

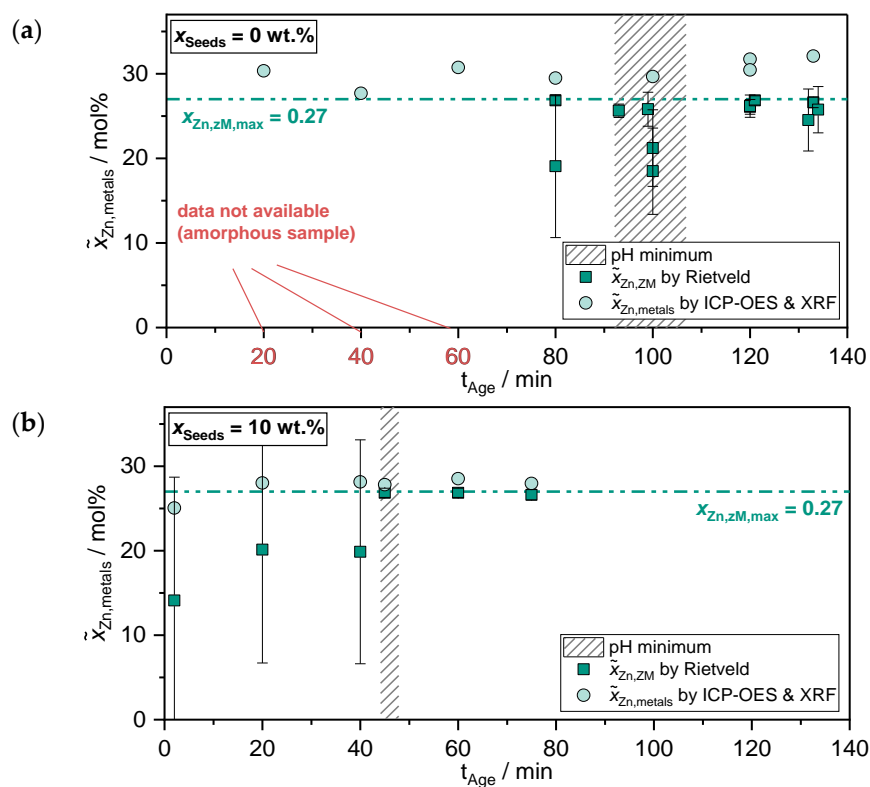


Figure 3. Evolution of the molar fraction of Zn in the metals of the solids samples (○) and in zincian malachite (□) as a function of the aging time t_{age} : (a) a standard aging process without seeding ($x_{Seeds} = 0$ wt.%), based on the work of Guse et al. [46]; (b) a preparation where seeds were added after co-precipitation is completed at $t_{age} = 0$ min ($x_{Seeds} = 10$ wt.%).

If seeds are added after precipitation is completed at $t_{\text{age}} = 0$ min ($x_{\text{seeds}} = 10$ wt.%), weakly noticeable peaks are present in the foremost amorphous diffractogram for $t_{\text{age}} \geq 2$ min in Figure 2b. For such low x_{seeds} values, the solid phase for $t_{\text{age}} \rightarrow 0$ consists of only a very limited amount of crystalline material, mostly freshly precipitated amorphous precursor, which explains the mostly amorphous diffractogram. Accordingly, for aging times below the necessary phase change time established by the pH minimum, there are some deviations for x_{zm} from the target of $x_{\text{zm}} \geq 95\%$ and for $\bar{x}_{\text{Zn,zm}}$ from $\bar{x}_{\text{Zn,zm}} = 0.27$, similar to the unseeded cases shown in Figure 3b. Again, $x_{\text{Zn,total}}$ in the solid phase is constant over the aging time, implying that the phase transformation proceeds by the restructuring of an amorphous Cu/Zn-based solid phase. On the basis of the FT-IR analysis (cf. the Supplementary Materials) and the literature [36,51], zincian georgeite is the most probable phase. After the phase change at $t_{\text{age}} = 45 \pm 2$ min, all further samples show $x_{\text{zm}} \geq 95\%$ and $\bar{x}_{\text{Zn,zm}} = 0.27$. This confirms that seeding accelerates the induction time until the phase change to zincian malachite takes place (t_{change}) and, consequently, accelerates the whole aging process significantly.

The correlation between the seeding mass fraction applied (x_{seeds}) and t_{change} is summarized in Figure 4. According to the literature, the total surface area of the seed material is key in the promotion of secondary nucleation [66,67]. However, the seed mass can be quantified much more precisely than the true available surface area of the seeds. Thus, we use x_{seeds} for the main portion of our studies but can confirm that the freshly prepared seed suspension had the same particle size distribution (PSD) for each experiment (cf. Section 2.1.3). The influence of particle size and, thus, surface area is then discussed separately in Section 2.1.3.

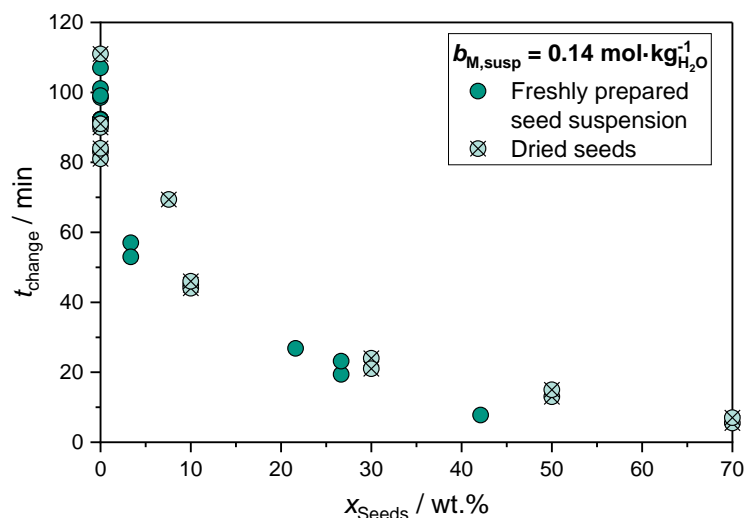


Figure 4. Necessary aging time until the phase change is completed (t_{change}) as a function of the seed mass fraction x_{seeds} for two different seeding methods.

The studies were conducted for the two seeding methods described in Section 3.2, using a seed suspension that had been aged shortly beforehand and previously dried seeds that were stored for up to one month. Without seeding, a mean aging time of $t_{\text{change}} = 94 \pm 9$ min is necessary until the phase transformation is completed. For both seeding methods, an increase in the seed mass fraction x_{seeds} resulted in a decreasing t_{change} value. Already, when $x_{\text{seeds}} = 3$ wt.%, the necessary time was reduced by 41% when applying the freshly prepared seed suspension. Higher x_{seeds} values led to increasingly short phase change times, resulting in $t_{\text{change}} = 8$ min for the highest seeding mass fraction considered ($x_{\text{seeds}} = 42$ wt.%). Using previously dried and subsequently resuspended seeds resulted in a slightly diminished effect. However, phase change times between $t_{\text{change}} = 46$ min and $t_{\text{change}} = 6$ min were achieved for seed mass fractions of between 10% and 70%, respectively. We explain the difference in effectiveness of the two seed methods

with the larger mean particle size and smaller mass-specific surface area of the dried seeds compared to the fresh seed suspension which is discussed in Section 2.1.3. According to Zander et al., the phase transformation occurs via the liquid phase [48]. Thus, a larger surface area, e.g., when more seeds with the same diameter are present, may explain the increasingly rapid transformation. In summary, both methods confirm the trend found by Gldenpfennig et al., with a simplified model system at milliliter scale [47], for the ternary Cu/ZnO/ZrO₂ catalyst preparation at laboratory scale in our investigation, proving that the necessary aging times decrease significantly when adding seeds.

2.1.2. Space-Time Yield

The effect of seeding on the necessary aging time was investigated for a low concentrated suspension (cf. Section 2.1.1) and a high concentrated suspension ($x_{\text{solids}} = 6 \text{ wt.}\%$). In the case of a high concentration, the metal salt molality in feed 2 was set to $b_{M,\text{Feed}2} = 0.86 \text{ mol}\cdot\text{kg}_{\text{H}_2\text{O}}^{-1}$ in order to evaluate if the findings were transferable to more industrially relevant solids concentrations. In Figure 5, the correlation between the seed mass fraction x_{seeds} and the necessary aging time required until phase change is completed (t_{change}) has been plotted for experiments using freshly prepared seed suspension. Furthermore, the effect of repeated seeding steps with a focus on a continuously operated aging step was also investigated. For this purpose, a defined amount of the aged suspension was maintained in the reactor after aging was completed in a first run and was further used as the seed suspension for a subsequent aging process. This procedure was then repeated up to five times.

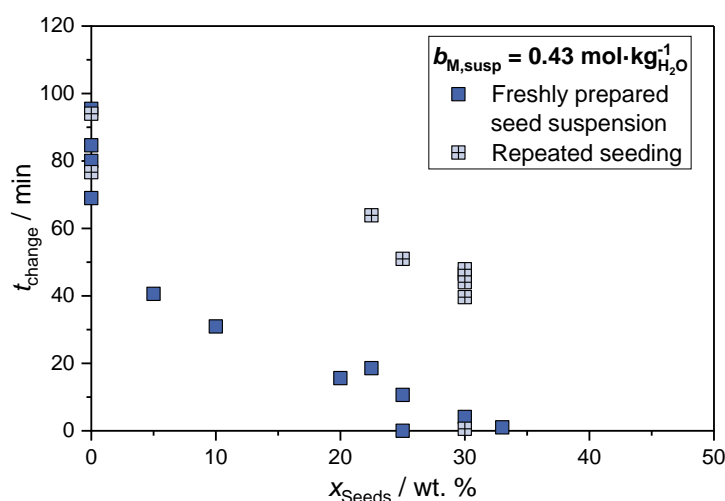


Figure 5. Necessary aging time until the phase change is completed (t_{change}) as a function of the seed mass fraction x_{seeds} at high reactant concentrations ($b_{M,\text{Feed}2} = 0.86 \text{ mol}\cdot\text{kg}_{\text{H}_2\text{O}}^{-1}$) when seeding is carried out once and, respectively, repeatedly.

Similar to studies of low metal salts molality ($b_{M,\text{susp}} = 0.14 \text{ mol}\cdot\text{kg}_{\text{H}_2\text{O}}^{-1}$), the necessary aging times decreased from $t_{\text{change}} = 83 \pm 9 \text{ min}$ for the unseeded approach to $t_{\text{change}} = 46 \text{ min}$ for $x_{\text{seeds}} = 5 \text{ wt.}\%$ and even an instantaneous phase change when the precipitate and the seed suspension mix are at $x_{\text{seeds}} \geq 30 \text{ wt.}\%$. The increased impact on the aging time compared to the lower concentration may result from a higher number of solid particles in the suspension and, thus, a higher collision frequency similar to contact-mediated nucleation processes [68,69].

When seeding with $x_{\text{seeds}} = 30 \text{ wt.}\%$ is applied repeatedly, the aging time increases to 36 to 53 min, compared to a stand-alone seeding run with one outlier at 4 min. Analysis of the particles by XRD (cf. Section 2.2.1) provided no explanation for this phenomenon. Yet, when compared to the unseeded scenario, the aging time was still reduced by 54% on average. The space-time-yield Y_{ST} , as defined in Equation (3), is introduced to evaluate the impact of seeding for the different seeding methods and the seed mass fraction. This way,

the reduced available reactor volume, as a major disadvantage of seeding with a freshly prepared suspension, is considered. Furthermore, only the mass of the freshly formed particles $\Delta m_{\text{dried aged precursor}}$ is considered in the balance. The mass of the added seeds m_{seeds} is excluded.

$$Y_{\text{ST}} = \frac{\Delta m_{\text{dried aged precursor}}}{t_{\text{change}} \cdot V_{\text{reactor}}} = \frac{m_{\text{solids, total}} - m_{\text{seeds}}}{t_{\text{change}} \cdot V_{\text{reactor}}} \quad (3)$$

The effect of the various seeding methods on the space-time-yield Y_{ST} for the two metal salt molalities investigated is summarized in Figure 6.

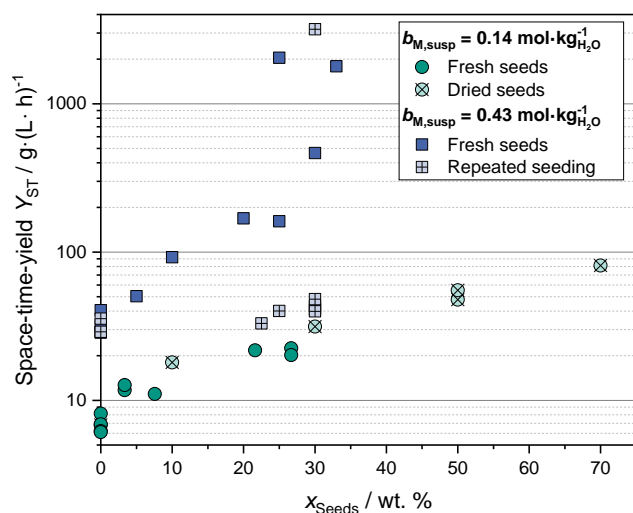


Figure 6. Space-time-yield of the aging process as a function of the seed mass fraction x_{Seeds} for the different seeding methods.

In general, each seeding approach increases the space-time-yield Y_{ST} . Despite the effectively reduced reactor volume, larger seed mass fractions result in a higher Y_{ST} with no apparent limit. As is to be expected, the data also confirm that adding seeds does not shift the solid–liquid equilibrium so that no additional metal ions remain in solution. Interestingly, the effect of seeding on Y_{ST} exceeds the effect of adjusting the reactant concentration from $b_{\text{M,Feed2}} = 0.27 \text{ mol} \cdot \text{kg}_{\text{H}_2\text{O}}^{-1}$ to $b_{\text{M,Feed2}} = 0.86 \text{ mol} \cdot \text{kg}_{\text{H}_2\text{O}}^{-1}$ which is, furthermore, limited by the solubility of the reactant salts.

The most significant improvement is evident for $x_{\text{seeds}} \approx 30 \text{ wt.}\%$ and $b_{\text{M,susp}} = 0.43 \text{ mol} \cdot \text{kg}_{\text{H}_2\text{O}}^{-1}$, where the space-time-yield is increased by a factor of up to 60. Here, space-time-yields of more than 2 kg of aged precursor material per hour and liter reactor volume were achieved. When seeding is conducted repeatedly, Y_{ST} decreases in accordance with the results discussed above but remains 5% larger than it would be without seeding. In one exceptional case, the high Y_{ST} was maintained for reasons that are not yet understood. For the usage of dried seeds at $b_{\text{M,susp}} = 0.14 \text{ mol} \cdot \text{kg}_{\text{H}_2\text{O}}^{-1}$, the space-time-yield was reproducibly increased by a factor of 12 for the highest seed mass fraction applied, making it a reliable alternative to the use of fresh seed suspension, where a similar increase in the space-time-yield is achieved. In summary, the vast reduction of necessary aging time when seeding is applied at low concentrations has also been confirmed for concentrated reactant solutions ($b_{\text{M,susp}} = 0.43 \text{ mol} \cdot \text{kg}_{\text{H}_2\text{O}}^{-1}$), where the impact on the space-time-yield is even higher.

2.1.3. Seed Surface Area

As stated previously, the impact of seeding is, in general, attributed to the total available surface area of the seeds [66,67]. The effective surface area of the seeds dispersed in the suspension can only be estimated, for instance, based on dynamic light scattering (DLS)

measurements, as shown in Figure 7b, or by BET analysis of the dried material. Thus, we mainly use the seed mass fraction x_{seeds} to quantify our results but have confirmed with DLS studies that the particle size distributions (PSD) of the applied seed particles are identical in each study. In Figure 7a, the PSD and standard deviations of the freshly prepared seed suspensions (“freshly prepared seeds”), as well as the PSD and deviations of the dried, fractionated and then resuspended seeds (“ $x < 40 \mu\text{m}$ ”), are compared. Additionally, the PSD of two larger-sized fractions of dried and resuspended seeds are investigated.

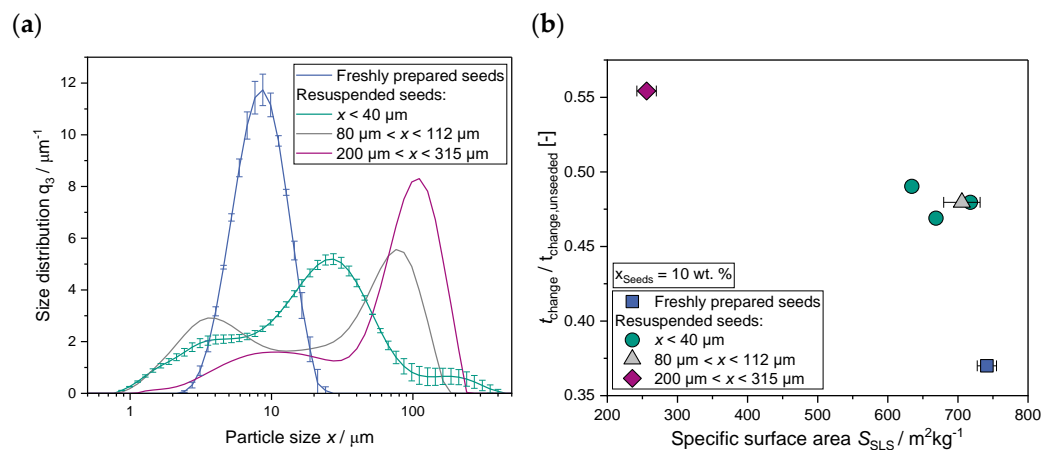


Figure 7. Correlation between the particle size distribution of seed particles and the impact on the necessary aging time: (a) mean particle size distribution of freshly prepared seed suspensions and of resuspended dried seeds with three different sieving fractions; (b) influence of the seed particle size on the necessary aging time in relation to the aging time without seeding.

For the freshly prepared seeds, as well as the dried and resuspended seeds, deviations across all the samples examined ($N > 10$) were negligibly small, confirming that x_{seeds} is a valid parameter by which to quantify the influence of seeding. However, the PSD of the previously dried seeds was multimodal and shifted toward larger particle sizes, despite their sieve fraction of $x < 40 \mu\text{m}$. The small particle fractions of $x < 2 \mu\text{m}$ and the large fractions of $x \gg 20 \mu\text{m}$ are probably a result of resuspending the particles with a disperser, along with the subsequent agglomeration of not thoroughly wetted particles [70]. This shift in PSD also explains why the necessary aging time when using dried seeds is slightly larger than for freshly prepared seeds (cf. Figure 4).

Next, the sieve fraction was shifted toward larger particle sizes, in order to investigate if, at a constant x_{seeds} , the variation of the PSD and, thus, the reduction of the mass-specific surface area negatively affected the impact of seeding on the necessary aging time t_{change} . It is evident from Figure 7a that larger sieve fractions do indeed lead to a shift in the PSD of the resuspended particles to even larger particle sizes, with second peaks at $x \approx 80 \mu\text{m}$ and $x \approx 110 \mu\text{m}$. Complementary to the PSD, the mass-specific surface area of the seeds in the suspension S_{SLS} was determined according to Equation (4), with the data from the static light scattering measurements and the density of malachite $\rho_{\text{ZM}} = 4.0 \text{ g}\cdot\text{cm}^{-3}$ as the main component [71]. The resulting surface areas are used in Figure 7b to analyze the correlation between S_{SLS} and the reduction in aging time, which is expressed as the ratio between the necessary aging time with seeding t_{change} and without seeding $t_{\text{change,unseeded}}$ under the same conditions.

$$S_{\text{SLS}} = \frac{6}{\rho_{\text{ZM}}} \frac{\sum V_i}{V_{\text{tot}}} = \frac{6}{\rho_{\text{ZM}}} \sum \left(\frac{q_{3,i} \Delta x_i}{x_i} \right) \quad (4)$$

It is evident from Figure 7b that at a constant x_{seeds} value, higher surface areas do result in a greater reduction in the necessary aging time. This confirms the hypothesis that the total surface area of seeds is a crucial variable for describing seeding and is, therefore, to be considered complementary to the mass fraction of seeds, especially if the PSD changes.

2.2. Catalyst Properties and Performance

A key question in the evaluation of whether seeding is a decisive tool for the preparation of catalysts is if the physicochemical data of the aged particles and, therefore, the product properties and quality are negatively affected by the reduced aging times, as is the case for an unseeded preparation [72,73]. Thus, the influence of seeding on both the physicochemical properties of the aged precursor and the pre-catalyst, as well as on the performance of the final catalyst in methanol synthesis, is evaluated in subsequent sections.

2.2.1. Physicochemical Properties of the Precatalyst

In Figure 8a, the influence of the seed mass fraction x_{seeds} and, consequently, of increasingly reduced aging times on the phase composition of the aged precursor is investigated. Additionally, the impact on phase composition after calcination is considered in Figure 8b. In both cases, X-ray diffractograms were evaluated by Rietveld refinement (cf. the Supplementary Materials). In each case, a relative error of $X^2 < 3$ between the measured and calculated diffraction pattern was obtained in the Rietveld refinement.

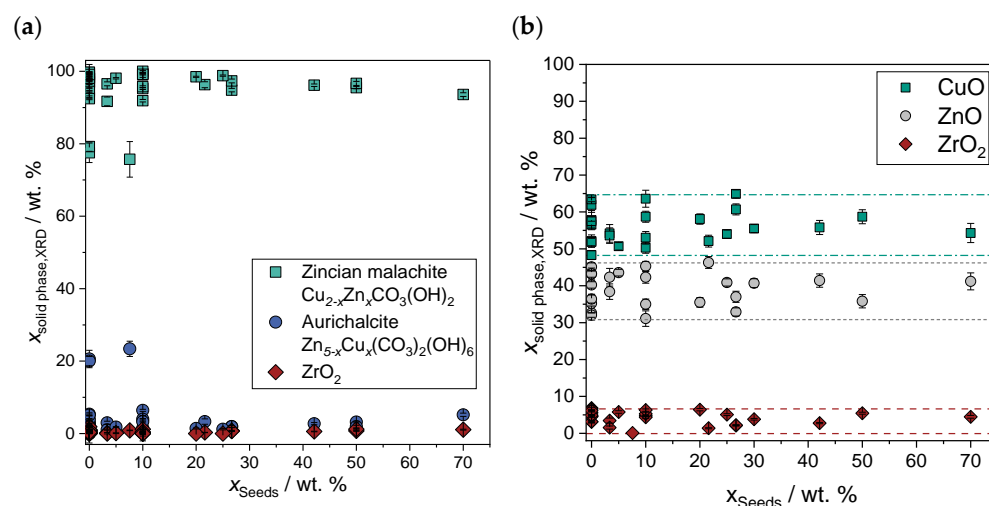


Figure 8. Solid phase composition of (a) the aged precursor and (b) the pre-catalyst as a function of the seeding mass fraction, as determined by XRD and Rietveld refinement.

After aging, zincian malachite is the main crystalline phase with mass fractions of, in general, $x_{\text{ZM}} > 90$ wt.%, independent of x_{seeds} . The two outliers are the result of insufficient temperature control, resulting in $T > 65$ °C. Aurichalcite is the second main crystalline phase, with $x_{\text{aur}} \approx 5$ wt.% due to the high Zn fractions of $\tilde{x}_{\text{Zn,metals}} > 0.27$ in the metal composition of the reactants. According to the Rietveld refinement, ZrO_2 has mass fractions of $x_{\text{ZrO}_2} < 2$ wt.%, due to the reduced molar mass compared to the other two phases. The independence of the phase composition from x_{seeds} confirms that the aging parameters and reactant ratios were chosen correctly and, more importantly, that despite reduced aging times, seeding does not affect the phase composition. This conclusion is confirmed by the analysis of the calcined material shown in Figure 8b where, again, no correlation between the phase composition and the seed mass fraction is evident. The higher fluctuation in the mass fractions determined by Rietveld refinement results from the overlap of the phase-specific diffraction patterns (cf. the Supplementary Materials).

Zincian malachite is the desired main phase after aging, due to its positive influence on the distribution of Cu and Zn crystallites at the nanoscale in the calcined pre-catalyst, as well as on the particle morphology [21,22,25–27]. Accordingly, TEM and TEM-EDXS images of an unseeded ($x_{\text{seeds}} = 0$ wt.%, $t_{\text{age}} = 122$ min) and a seeded preparation ($x_{\text{seeds}} = 30$ wt.%, $t_{\text{age}} = 55$ min) are compared in Figure 9 to investigate if these two properties are also unaffected by seeding and the resulting reduction in aging time. Additionally, an unseeded preparation with a comparably short total aging time ($t_{\text{age}} = 60$ min) is considered as a reference to validate

if seeding is indeed necessary for the preservation of certain physicochemical properties or if a reduction in aging time alone would be a valid, but simpler, alternative after all.

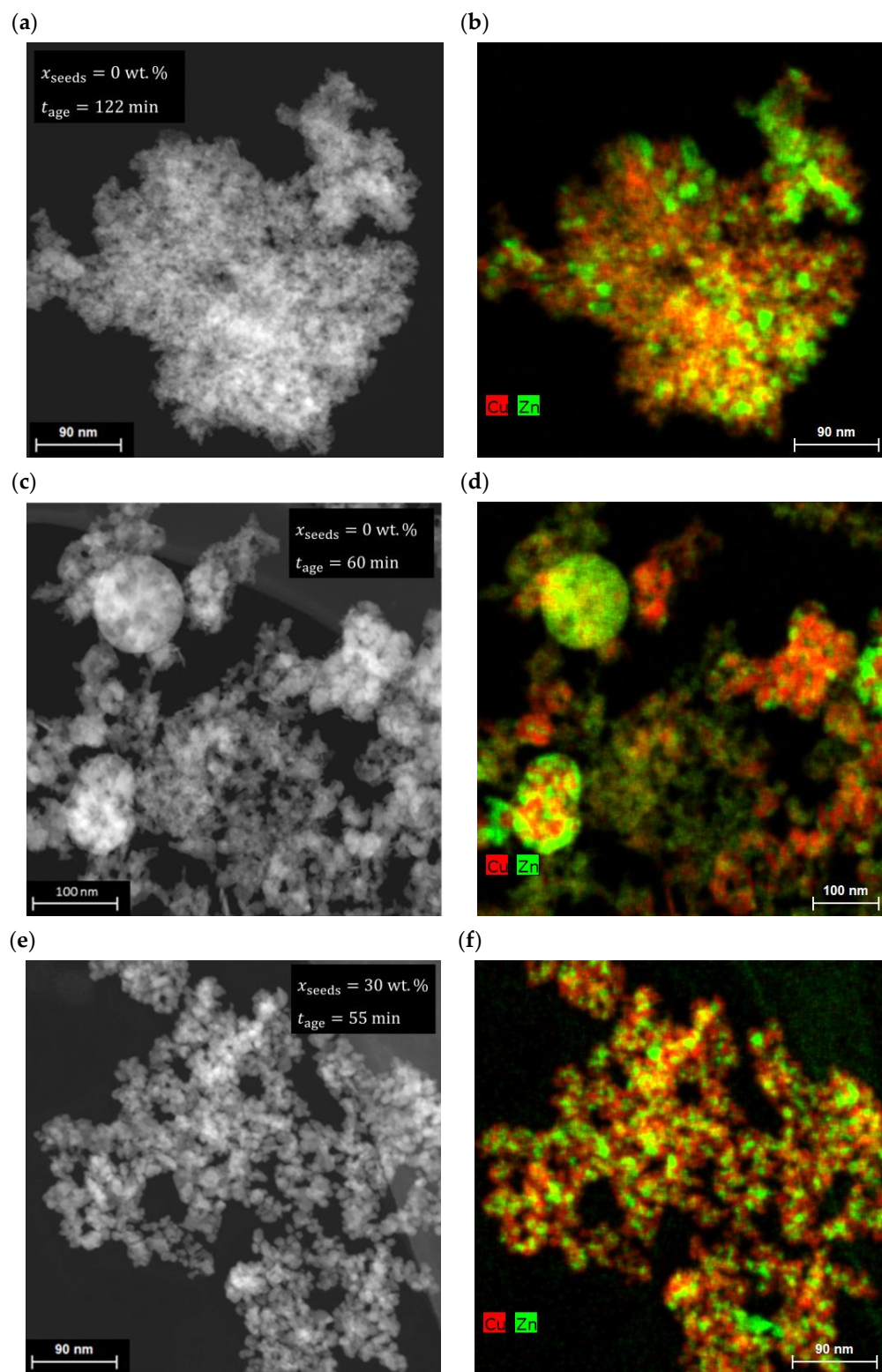


Figure 9. TEM and TEM-EDXS images of the calcined precatalysts. (a,b): unseeded preparation ($x_{seeds} = 0$ wt.%, $t_{age} = 122$ min); (c,d): unseeded preparation with a shortened aging ($x_{seeds} = 0$ wt.%, $t_{age} = 60$ min); (e,f): seeded preparation ($x_{seeds} = 30$ wt.%, $t_{age} = 55$ min). Cu is marked in red and Zn is marked in green.

In the TEM images on the left, a similar particle size distribution and morphology are evident for all samples. Single spherical particles are aggregated into a mesh-like entity. In the unseeded preparation where $t_{\text{age}} = 122$ min, the mesh seems denser. We believe that this is an artifact of the sample preparation for TEM imaging since the quantitative results shown in Table 1 show no significant deviation between the unseeded and seeded samples. In the unseeded preparation with a reduced aging time, large spherical particles are additionally present.

Table 1. Selected physicochemical properties of the precatalysts from unseeded and seeded experiments for $b_{\text{M,Feed2}} = 0.27 \text{ mol} \cdot \text{kg}_{\text{H}_2\text{O}}^{-1}$, aged for the specified total process time t_{age} .

x_{seeds} [wt.%]	t_{age} [min]	$\bar{x}_{\text{Cu,metals}}$ [mol%]	$\bar{x}_{\text{Zn,metals}}$ [mol%]	$\bar{x}_{\text{Zr,metals}}$ [mol%]	$\bar{x}_{\text{CuO,XRD}}$ [nm]	$\bar{x}_{\text{Pore,BJH}}$ [nm]	S_{BET} [m ² g ⁻¹]	S_{Cu} [m ² g ⁻¹]
0	122 ± 6	63.2 ± 0.8	28.4 ± 0.9	8.4 ± 0.4	3 ± 1	10 ± 1	122 ± 4	68
0	60	65.7	24.0	9.1	9 ± 0	31	69	46
3	85 ± 2	59.1	32.1	8.7	3 ± 0	9 ± 0	123 ± 1	- *
10	78 ± 1	65.3	26.8	7.9	4 ± 0	- *	- *	- *
27	51 ± 2	64.3	28.4	7.2	2 ± 0	11	120	- *
30	55 ± 2	64.4	27.1	8.5	3 ± 0	9	148	66
50	14 ± 1	64.1	26.8	9.0	4 ± 0	- *	- *	- *
70	7 ± 1	64.3	26.8	7.9	4 ± 0	11	126	- *

* No data available due to limited resources.

The TEM-EDXS evaluation on the right indicates that these spheres are composed of CuO alone, with minuscule traces of ZnO. Furthermore, multiple clusters of ZnO where $x > 100$ nm are present. These inhomogeneities indicate that the formation of zincian malachite during aging, as a prerequisite for homogeneous Cu/Zn distribution [36], was not complete at the time of sampling. The evolution of the X-ray diffractogram during the unseeded aging shown in Figure 2 confirms this assumption. In contrast, for both the unseeded and the seeded samples, the aging time t_{age} exceeded the necessary phase change time t_{change} . As a result, the homogeneous distribution of Cu and Zn is present for these two samples, confirming, first, the necessity of forming zincian malachite during aging, and second, the importance of seeding to reduce the necessary aging time while maintaining the product specifications. The Zr distribution depicted in the Supplementary Materials (Figure S5) shows no deviating trends and is, therefore, not separately discussed here.

Complementary to the visual results, Table 1 provides an overview on how seeding influences the key properties of the resulting precatalyst quantitatively. Again, an unseeded preparation with a reduced aging time ($t_{\text{age}} = 60$ min) is included as a reference for low-quality material. The mean values and standard deviations for several unseeded samples with a sufficiently long aging time to complete the phase change ($t_{\text{age}} = 122$ min) are included as a reference for a material that meets the specifications for a high-quality catalyst.

The metal composition is largely independent of the preparation method. Small deviations in the range of ± 1 wt.% result from the accuracy of the measurement itself (cf. Section 3.3). However, reducing the aging times without applying seeding will result in a major increase in the mean CuO crystallite size $\bar{x}_{\text{CuO,XRD}}$, as determined by Rietveld refinement, by a factor of three. This is in agreement with the inhomogeneous distribution of Cu and Zn, which is evident in the TEM-EDXS images showing large clusters of CuO. The increased crystallite size also decreases the mass-specific surface area S_{BET} and the copper surface area S_{Cu} by a factor of around two. Furthermore, the pore size is tripled. This negative effect of reduced aging time on the sample properties matches the correlations described in the literature.

In contrast, while the aging time is also decreased significantly for the seeded samples, in some cases down to just 7 min, no negative impact on any physicochemical property examined herein is evident. This trend is confirmed by a TPR study (cf. Figure S6 in the Supplementary Materials), which resulted in a maximum value of the reduction temper-

ature of $T_{\text{red,max}} = 175$ °C for both the unseeded preparation with $t_{\text{age}} = 122$ min and the seeded preparation ($x_{\text{seeds}} = 30$ wt.%). This maximum is, generally, attributed to the reduction of bulk Cu(II)O to Cu(0) [74]. For the unseeded experiment where $t_{\text{age}} = 60$ min, the reduction is shifted toward higher temperatures, where $T_{\text{red,max}} = 184$ °C. This shift generally results from larger crystallites [43] and is, therefore, in agreement with the data discussed above.

In summary, all the key physicochemical properties examined are similar for seeded and unseeded preparations if the condition $t_{\text{age}} > t_{\text{change}}$ is true. This is valid even if the aging time is reduced to only 10% of the aging time of the unseeded preparation. However, reducing the aging time without applying seeding will result in subpar properties, especially regarding the homogeneity of the precatalyst and the surface properties.

2.2.2. Comparison of Catalytic Behavior

Based on the previously discussed analytical results for the precatalysts and the known correlations between physicochemical properties and catalyst quality in the literature [26,43], there should be no impact of seeding on the catalyst's performance in methanol synthesis. This hypothesis is first discussed on the basis of the mean methanol productivity P_{MeOH} over 50 h on stream in the experimental set-up described in Section 3.4:

$$P_{\text{MeOH}} = \frac{\dot{m}_{\text{MeOH,out}}}{V_{\text{catalyst}}} = \frac{\dot{m}_{\text{MeOH,out}}}{m_{\text{catalyst}} \cdot \rho_{\text{bulk}}^{-1}} \quad (5)$$

P_{MeOH} is plotted in Figure 10 for two different feed gas compositions and four different catalysts. Besides the three materials discussed above, the performance of a commercially available Cu/ZnO/Al₂O₃ catalyst is used for comparison.

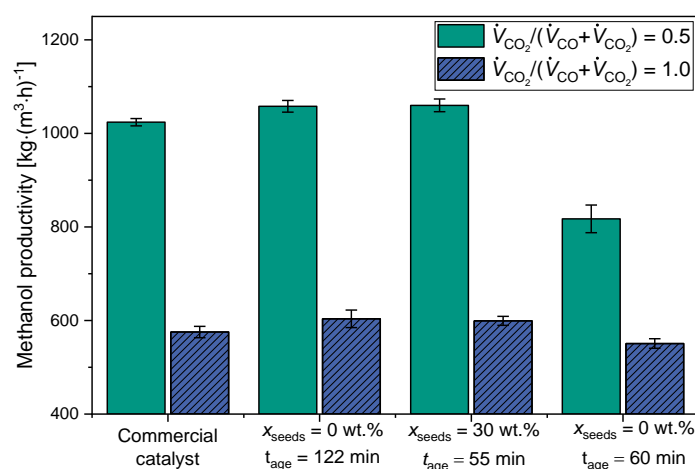


Figure 10. Influence of seeding and a reduced aging time on the mean methanol productivity over 50 h on stream and in comparison with a commercially available catalyst for two CO₂/CO inlet ratios at 30 bar and GHSV: 4.41 s⁻¹. $T = 230$ °C for $\dot{V}_{\text{CO}_2} / (\dot{V}_{\text{CO}_2} + \dot{V}_{\text{CO}}) = 0.5$ and $T = 250$ °C for $\dot{V}_{\text{CO}_2} / (\dot{V}_{\text{CO}_2} + \dot{V}_{\text{CO}}) = 1.0$.

For a feed gas composed of equivolumetric amounts of CO and CO₂ ($\dot{V}_{\text{CO}_2} / (\dot{V}_{\text{CO}_2} + \dot{V}_{\text{CO}}) = 0.5$), the methanol productivity is identical for the unseeded ($x_{\text{seeds}} = 0$ wt.%) and seeded catalyst ($x_{\text{seeds}} = 30$ wt.%) if the total aging time exceeds the necessary time to complete the phase change: $t_{\text{age}} = 122$ min and $t_{\text{age}} = 55$ min, respectively. In both cases, P_{MeOH} is 3–4% larger than the productivity of the commercial state-of-the-art catalyst with the additives required for shaping. This shows that seeding allows the production of catalytic material with competitive product quality at a much higher space-time yield than previously reported in the open literature (cf. Section 2.1.2). As is to be expected from the analytical results in Section 2.2.1, the productivity collapses to only 77% if the aging

time is reduced to $t_{\text{age}} = 60$ min without applying seeding. This finding is in agreement with the results from the literature [72,73]. The error bars show the fluctuation in P_{MeOH} over 50 h on stream after a running-in period of about 70 h, which is negligibly small in each case. Hence, none of the catalysts shows significant deactivation over the process time investigated.

Using a feed gas composed of H_2 and pure CO_2 ($\dot{V}_{\text{CO}_2}/(\dot{V}_{\text{CO}_2} + \dot{V}_{\text{CO}}) = 1.0$), the productivity drops to approx. 60% in each case. Accordingly, the absolute differences between the samples decrease. Nevertheless, the same trend prevails: the maximum P_{MeOH} is achieved with the seeded and unseeded catalyst that experienced a sufficiently long aging time, followed directly by the commercial catalyst, and, with a significant drop-off, the unseeded catalyst with a reduced aging time.

Additionally, the impact of the preparation on the CO_x conversion X_{CO_x} according to Equation (6) and the methanol selectivity S_{MeOH} according to Equation (7) are examined in Figure 11.

$$X_{\text{CO}_x} = \frac{\dot{n}_{\text{CO},\text{in}} - \dot{n}_{\text{CO},\text{out}} + \dot{n}_{\text{CO}_2,\text{in}} - \dot{n}_{\text{CO}_2,\text{out}}}{\dot{n}_{\text{CO},\text{in}} + \dot{n}_{\text{CO}_2,\text{in}}} \quad (6)$$

$$S_{\text{MeOH}} = \frac{\dot{n}_{\text{MeOH},\text{out}}}{\sum v_x \dot{n}_{\text{C}_x\text{O}_y\text{H}_z,\text{out}}} \quad (7)$$

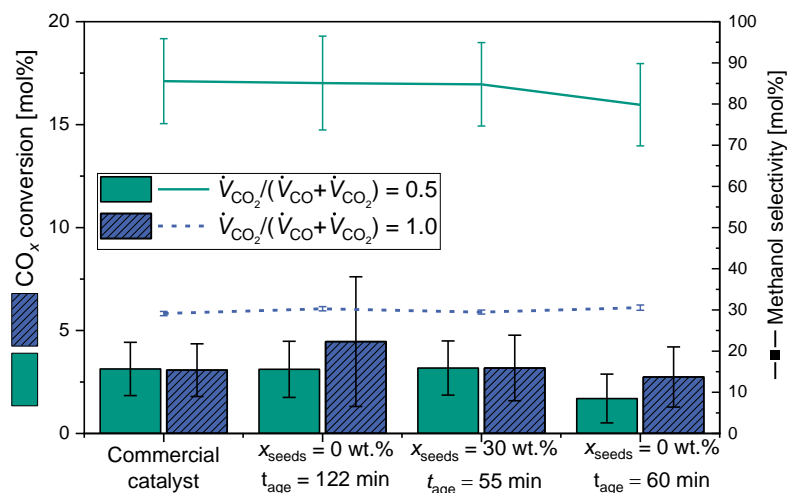


Figure 11. Influence of seeding and a reduced aging time on CO_x conversion and methanol selectivity, in comparison with one commercially available catalyst for two CO_2/CO inlet ratios at 30 bar and GHSV: 4.41 s^{-1} . $T = 230 \text{ }^\circ\text{C}$ for $\dot{V}_{\text{CO}_2}/(\dot{V}_{\text{CO}_2} + \dot{V}_{\text{CO}}) = 0.5$ and $T = 250 \text{ }^\circ\text{C}$ for $\dot{V}_{\text{CO}_2}/(\dot{V}_{\text{CO}_2} + \dot{V}_{\text{CO}}) = 1.0$.

All four catalysts investigated show the same methanol selectivity. For $\dot{V}_{\text{CO}_2}/(\dot{V}_{\text{CO}_2} + \dot{V}_{\text{CO}}) = 0.5$, a mean selectivity over 50 h on stream of 78% to 85% is reached. These amounts are comparable to past studies using similar process parameters [15]. In parallel, H_2O is formed by the reverse water-gas shift reaction from CO_2 and H_2 [15]. For a pure CO_2 feed gas, the selectivity is lowered to approx. 30% for each catalyst. This results from a shift in the water-gas-shift reaction caused by the large amounts of CO_2 and the simultaneous absence of CO in the gas phase, resulting in increased H_2O formation. Further possible influences are the higher temperature and an ongoing deactivation of the catalyst. For similar materials, an ongoing, partial deactivation has been detected for more than 500 h on stream [15,75]. In summary, all four catalysts analyzed here behave similarly in terms of selectivity. Thus, the phase composition after successful aging as well as seeding does not seem to influence methanol selectivity.

In contrast, the conversion of CO and CO_2 behave similarly to the methanol productivity shown in Figure 10: for both feed gas compositions, the conversion X_{CO_x} is similar for the commercial catalyst and for both catalysts prepared with a sufficiently long aging time.

The increased CO_x conversion of the unseeded catalyst for $\dot{V}_{\text{CO}_2}/(\dot{V}_{\text{CO}_2} + \dot{V}_{\text{CO}}) = 1.0$ most probably results from some fluctuation in the measurements, as indicated by the increased standard deviations compared to the other samples. These fluctuations are explainable by slight condensation after the reactor outlet [76]. However, for the unseeded catalyst with a reduced aging time, the CO_x conversion is decreased by approx. 45% and 12%, respectively. This trend explains the decreased methanol productivity of the catalyst in Figure 10.

Altogether, the starting hypothesis that seeding does not influence the properties of the precatalyst and, therefore, should also not influence the performance of the catalyst in methanol synthesis if $t_{\text{age}} > t_{\text{change}}$ is fulfilled, is confirmed.

3. Materials and Methods

3.1. Reactants and Intermediates

The reactant solutions were prepared from $\text{Cu}(\text{NO}_3)_2 \cdot 3\text{H}_2\text{O}$ (purity $\geq 99.5\%$, Merck, Darmstadt, Germany), $\text{Zn}(\text{NO}_3)_2 \cdot 6\text{H}_2\text{O}$ (purity $\geq 99\%$, Alfa Aesar, Ward Hill, MA, USA), $\text{ZrO}(\text{NO}_3)_2 \cdot 6\text{H}_2\text{O}$ (purity $> 99\%$, Sigma-Aldrich, Darmstadt, Germany), NaHCO_3 (purity $\geq 99\%$, Carl Roth, Karlsruhe, Germany) or, if stated, Na_2CO_3 (purity $\geq 99\%$, Carl Roth, Karlsruhe, Germany), and demineralized water. In some studies, a HNO_3 solution (65%, Carl Roth) and NaOH (purity $\geq 99\%$, Carl Roth, Karlsruhe, Germany) were used to adjust the initial pH after co-precipitation.

We differentiate the following four intermediates: (1) the co-precipitate directly after co-precipitation is completed ($t_{\text{age}} = 0$ min); (2) time samples taken at defined moments (t_{age}) during aging; (3) the aged precursor after aging is completed; and (4) the precatalyst consisting of CuO , ZnO and ZrO_2 , as obtained by calcination of the aged and dried precursor.

3.2. Experimental Setup and Procedure

On the basis of previous studies on the influence of mixing in co-precipitation and the overlapping of co-precipitation and aging [35], continuous co-precipitation and batch aging were strictly separated according to Figure 12 [35,46]. A NaHCO_3 or Na_2CO_3 solution (feed 1) and a metal nitrate solution (feed 2) with equal volume flows were continuously mixed in an impinging micro jet mixer, where co-precipitation then took place. Two gear pumps (GB-P23-DEELE, Micropump, Avenue Vancouver, WA, USA) working in combination with magnetic-inductive flow meters (IFC90, Krohne, Duisburg, Germany) were used at constant total volume flow rates of $\dot{V}_{\text{Feed1}} = \dot{V}_{\text{Feed2}} = 300 \pm 15 \text{ mL} \cdot \text{min}^{-1}$. The reactant vessels, the feed tubes and the aging tank reactor were temperature-controlled, with $\pm 1 \text{ K}$ accuracy.

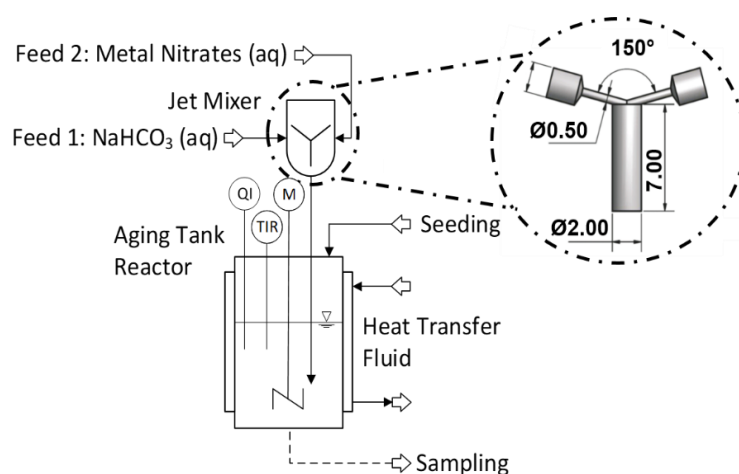


Figure 12. Experimental setup. M: motor, TCR: temperature control and recording, QR: pH recording. Dimensions are shown in mm. From Guse et al. [35,46].

The co-precipitate suspension was then fed directly into a double-jacketed 4000 mL glass tank reactor ($d_{\text{tank}} = 120$ mm) with four baffles, according to DIN 28131. Aging took place under stirring with a two-staged three-blade propeller agitator ($d_{\text{stirrer},1} = 40$ mm; $d_{\text{stirrer},2} = 50$ mm, 30° pitch) running at 1000 rpm. The pH was measured with a HI1190T electrode (Hanna, Woonsocket, RI, USA). Samples during aging were obtained by withdrawing 30–50 mL of suspension near the stirrer through the bottom outlet. Aging was terminated between 15 min and 60 min after a pH minimum had been achieved [46] to ensure that the phase change was completed in the high-concentration studies wherein mixing during aging was sub-par.

All low-concentration experiments ($x_{\text{solids}} = 2$ wt%, $b_{\text{M,Feed2}} = 0.27$ mol·kg $_{\text{H}_2\text{O}}^{-1}$) at $\text{pH}(t_{\text{age}} = 0 \text{ min}) = 6.7$ were conducted, where $T = 55$ °C, $b_{\text{NaHCO}_3,\text{Feed1}} = 1.018$ mol·kg $_{\text{H}_2\text{O}}^{-1}$, $b_{\text{Cu}(\text{NO}_3)_2,\text{Feed2}} = 0.162$ mol·kg $_{\text{H}_2\text{O}}^{-1}$, $b_{\text{Zn}(\text{NO}_3)_2,\text{Feed2}} = 0.081$ mol·kg $_{\text{H}_2\text{O}}^{-1}$, $b_{\text{ZrO}(\text{NO}_3)_2,\text{Feed2}} = 0.027$ mol·kg $_{\text{H}_2\text{O}}^{-1}$ and $X_{65\%\text{HNO}_3,\text{Feed2}} = 22$ mL·kg $_{\text{H}_2\text{O}}^{-1}$. The high-concentration experiments ($x_{\text{solids}} = 6$ wt%, $b_{\text{M,Feed2}} = 0.86$ mol·kg $_{\text{H}_2\text{O}}^{-1}$) were conducted, where $T = 55$ °C, $b_{\text{Na}_2\text{CO}_3,\text{Feed1}} = 0.889$ mol·kg $_{\text{H}_2\text{O}}^{-1}$, $b_{\text{Cu}(\text{NO}_3)_2,\text{Feed2}} = 0.516$ mol·kg $_{\text{H}_2\text{O}}^{-1}$, $b_{\text{Zn}(\text{NO}_3)_2,\text{Feed2}} = 0.258$ mol·kg $_{\text{H}_2\text{O}}^{-1}$ and $b_{\text{ZrO}(\text{NO}_3)_2,\text{Feed2}} = 0.086$ mol·kg $_{\text{H}_2\text{O}}^{-1}$. Here, the initial $\text{pH}(t_{\text{age}} = 0 \text{ min}) = 6.7$ was controlled by adjusting \dot{V}_{Feed2} during co-precipitation ($200 \text{ mL}\cdot\text{min}^{-1} \leq \dot{V}_{\text{Feed2}} \leq 300 \text{ mL}\cdot\text{min}^{-1}$), where $\dot{V}_{\text{Feed1}} = 300 \text{ mL}\cdot\text{min}^{-1} \pm 5 \text{ mL}\cdot\text{min}^{-1}$.

The suspensions of both the time samples and the aged precursor were collected without dilution for the analytics described in Section 3.3. They were then filtered (MN85/70, Macherey-Nagel, Duren, Germany) using a water aspirator or a vacuum pump. The filter cake was washed by displacement washing with demineralized water until an electrical conductivity of $<50 \mu\text{S}\cdot\text{cm}^{-1}$ (Profiline LF 197, WTW, Munich, Germany) was achieved and until no nitrate could be detected by nitrate test strips ($<10 \text{ mg}\cdot\text{L}^{-1}$, VWR Chemicals, Radnor, PA, USA). The moist sample was then dried at ambient pressure and at the aging temperature, or at $p \leq 10$ mbar and 35 °C, for at least 24 h. The chosen samples were then calcined as described elsewhere [43] and ground in a mortar until no more lumps were visually detected.

Suspensions of freshly prepared seeds were obtained by conducting aging until the pH minimum was reached and by then withdrawing the suspension until the desired volume of seeding suspension remained in the aging tank reactor. The freshly co-precipitated suspension was then added to the aged suspension in the aging tank reactor near the stirrer, as described above.

Dried seeding material was obtained by completing an unseeded aging process under the same conditions as in the intended seeding experiment and then washing, drying and mortaring the solids as described above for storage and analysis. For the seeding experiments, the seeds were fractionated (in general, $x < 40 \mu\text{m}$) using a sieve shaver (Retsch, ISO 9001, Haan, Germany) and then resuspended in 30 mL demineralized water for 5 min at $n = 9800 \text{ min}^{-1}$ with a disperser (IKA T 25 Ultra Turrax, Staufen, Germany). The seeding material was then added to the freshly co-precipitated suspension with a syringe, introduced from the top of the reactor directly after co-precipitation was finished ($t_{\text{age}} = 0 \text{ min}$). Seeding was completed within a maximum period of 2 min.

3.3. Analytics

The phase composition of the dried and ground solids was determined, using a combination of Fourier transform infrared spectroscopy (FT-IR) and X-ray diffraction (XRD) measurements to analyze both the amorphous and crystalline samples. The FT-IR spectra in the range of $4000 \text{ cm}^{-1} < \tilde{\nu} < 230 \text{ cm}^{-1}$, with a resolution of 2 cm^{-1} , were obtained using a Varian 660-IR spectrometer (Agilent, Santa Clara, CA, USA) in combination with the proprietary software Resolution Pro, adopting the KBr disk approach with approx. 3 mg sample and 300 mg KBr. Before each measurement, the chamber was purged for 5 min with N_2 to remove any CO_2 from the measuring chamber.

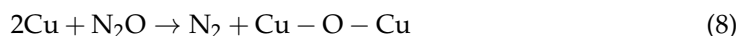
A Panalytical X'Pert Pro X-ray diffractometer with Bragg–Brentano geometry and Cu K- α radiation with a Ni filter was used for XRD testing in the range of $5^\circ < 2\theta < 80^\circ$ for 120 min. The mass fractions of the solid phases were determined using Rietveld refinement with Profex software, version 5.1 [77]. The reference data are given in the Supplementary Materials.

A Bruker Pioneer S4 was used to perform XRF measurements on the samples to determine their metal ratios [43]. A Vario EL cube and a Vario Micro Cube (both from Elementar Analysensysteme GmbH, Langenselbold, Germany) were used to determine the mass fractions of C, H and N by combustion analysis, coupled with thermal conductivity detection. A 725 ICP-OES spectrometer (Agilent, Santa Clara, CA, USA) and, alternatively, an iCAP 7000 (Thermo Scientific, Needham, MA, USA) were used for the ICP-OES measurements.

The specific particle surface areas (S_{BET}) were measured at 77.35 K using N_2 physisorption measurements in a Quantachrome NOVA 2000e device (Anton Paar, Ankerstraße, Graz, Austria). The samples were fractionated to particle sizes in the range of $250 \mu\text{m} \leq x \leq 500 \mu\text{m}$ and degassed for 20 h at 130 °C. Isotherms were analyzed using the Brunauer–Emmett–Teller model (BET) in the 0.004–0.98 p/p_0 range.

An Altamira AMI-300 device equipped with a thermal conductivity detector (TCD) was used for the combined temperature-programmed reduction (TPR) and N_2O pulse chemisorption analyses. For the TPR measurement, approx. 100 mg of the catalyst sample was placed in a U-shaped quartz reactor, dried and then cooled under argon. Then, the samples were heated from 50 °C to 250 °C at a rate of 1 K/min (250 °C, holding for 45 min) in a gas mixture containing 5 vol% H_2/Ar .

A rough determination of the active Cu surface of the catalysts can be performed via N_2O pulse chemisorption, according to the following reaction:



The controlled oxidation of the surface of the now reduced sample is conducted with N_2O by sending pulses of a definite volume (518 mL). The liberated N_2 is quantified with the cumulated data of the TCD and in comparison with a definite commercial gas mixture (5 vol% N_2 /Helium Air Liquide CRYSTAL gas Mixture). From the total amount of N_2 that is liberated, the oxidized surface of the catalysts can then be calculated. Further details on the TPR and N_2O pulse chemisorption procedure are given in the Supplementary Materials.

The particle morphology was analyzed by scanning electron microscopy (SEM), using a Zeiss Gemini SEM 500 with a Schottky field emission cathode. The particles of the dried sample were fixated on adhesive carbon pads. Transmission electron microscopy (TEM) imaging was realized with a FEI Osiris ChemiStem (200 kV) and energy-dispersive X-ray spectroscopy (EDXS, Cambridge, UK), using an equipped Bruker Quantax system (XFlash detector, Karlsruhe, Germany). The dried sample was suspended in water by means of an ultrasound bath and then spread on a TEM gold grid using an ultrasonic fogger.

The particle size distribution (PSD) of the seeds in the suspension was determined by a combination of dynamic light scattering (DLS), where the PSD of a possible fine fraction ($3 \text{ nm} \leq x \leq 3 \mu\text{m}$) is analyzed [78], and static light scattering (SLS) for the coarse fraction ($10 \text{ nm} \leq x \leq 3.5 \mu\text{m}$) [79,80]. The suspension was analyzed directly after preparation, respectively, with sampling ($\Delta t < 5 \text{ min}$). Further information can be found in the Supplementary Materials.

3.4. Methanol Synthesis

For analyzing the catalyst performance in methanol synthesis from syngas (45 vol% H_2 ; 35 vol% N_2 ; 20% CO_x), a six-fold parallel reactor system was used. The process has been described by Wild et al. in detail [81]. Each respective reactor contained one precatalyst sample and had the same volume flow distribution, as well as the same pressure and temperature. The feed gases of carbon monoxide (CO , 99.97 vol%), nitrogen (N_2 , 99.9999 vol%), hydrogen (H_2 , 99.9999 vol%) and a mixture of CO_2 and N_2 (50: 50 \pm 1.0 vol%) were supplied by Air Liquid Germany GmbH (Frankfurt, Germany). The precatalysts ($2 \pm 0.0005 \text{ g}$) were sieved

into a fraction of 250–500 μm , followed by physical mixing with 8.2715 ± 0.0002 g silicon carbide (SiC, Hausen Mineraliengroßhandel GmbH, Telfs, Tirol, Austria) of the same grain size, in order to prevent the formation of hotspots in the reactor. The beds were filled as fivefold stacks to ensure the adequate grain distribution of the components, with additional SiC layers at the top and bottom of the beds. The catalyst beds were 30 ± 2 mm in length, with a bulk density of $\rho_{\text{bulk}} = 0.8825$ g·mL⁻¹.

The experiments were performed at a constant pressure of 30 bar for a total process time of 176 h. The gas hourly space velocity (GHSV) used in these experiments was 4.41 s⁻¹. In addition, the volume fraction of CO₂ in relation to the total volume fraction of CO and CO₂ (CO₂/CO_x) in the syngas varied between CO₂/CO_x = 0.5 and CO₂/CO_x = 1.0. First, the plant was run with CO₂/CO_x = 0.5 at 230 °C for approx. 120 h. Of this duration, approx. 70 h were used for initialization and 50 h were used to evaluate the methanol productivity, selectivity and CO_x conversion of the different catalysts. Afterward, the process conditions were adjusted to CO₂/CO_x = 1.0 and 250 °C, and the same quantities were evaluated over a time on stream of approx. 45 h.

4. Conclusions

In summary, we confirmed both our two main hypotheses: first, seeding does reduce the necessary aging time until the completion of the phase change in Cu/Zn-based catalyst precursors to zincian malachite from $t_{\text{change}} > 80$ min to $t_{\text{change}} < 1$ min, even at solids concentrations as high as 6 wt.%. Second, the calcined precatalysts that were prepared following the seeding approach have similar physicochemical properties when compared to unseeded material preparation and show the same performance characteristics in terms of methanol synthesis.

The mass-specific surface area of the seeds and, if the particle size distribution is constant, the mass fraction of seeds in the suspension are the main factors that decrease the necessary aging time t_{change} . Seed mass fractions as low as $x_{\text{seeds}} = 3$ wt.% had already decreased t_{change} by more than 40%. Whether dried seeds or freshly prepared seeds were added and the way in which they were added [46] only had a minor impact in comparison. By applying seeding, the space-time yield of precipitation and aging was increased by a factor of up to 60. In principle, these results should be transferable to other catalyst materials that undergo a similar phase transformation during preparation.

A comparison of the precatalysts from seeded and unseeded preparations with comparably reduced aging time ($t_{\text{age}} \approx 60$ min) revealed that seeding is necessary to complete the phase change to zincian malachite within this reduced time frame. Otherwise, inhomogeneous material with a reduced surface area and, thus, reduced methanol productivity will result. The methanol productivity, CO_x conversion and methanol selectivity of a catalyst from a seeded preparation proved to be at least equivalent to the performance of both an unseeded material with a much longer aging time ($t_{\text{age}} \approx 120$ min) and a commercial Cu/ZnO/Al₂O₃ catalyst.

The exact mechanism that occurs during seeding is still a matter of debate and should be the focus of future studies so that seeding can be further optimized. However, our results complement the findings by Guldenpfennig et al. [47] and Guse et al. [46] and suggest that seeding reduces the induction period significantly. It is plausible that a contact-induced phase transformation by means of a template effect is involved. This would explain why increased x_{seeds} leads to a reduction in the required aging time, down to an instantaneous phase change if a critical seed mass is reached. The evaluation of timed samples by high-definition SEM imaging, e.g., samples prepared by cryo-quenching in liquid N₂ [82], would be a possible method for a future study. Additionally, we suggest more thorough performance tests of catalysts prepared with seeded aging for a final evaluation of long-term performance.

Based on our results, we highly recommend applying seeding as a standard tool in the preparation of Cu/Zn-based catalysts, in order to make the processes more economically and ecologically viable in the future, without any identifiable downsides.

Supplementary Materials: The supporting information can be downloaded at: <https://www.mdpi.com/article/10.3390/catal14080517/s1>. Figure S1. FT-IR spectra of the dried and washed samples as a function of aging time for: (a) a standard aging process without seeding ($x_{\text{Seeds}} = 0$ wt.%), (b) a preparation where seeds were added after co-precipitation is completed at $t_{\text{age}} = 0$ min ($x_{\text{Seeds}} = 10$ wt.%), (c) $x_{\text{Seeds}} = 30$ wt.% and (d) $x_{\text{Seeds}} = 70$ wt.%; Figure S2. SEM images of two aged precursors from an unseeded ($x_{\text{seeds}} = 0$ wt.%) (a,c) and a seeded ($x_{\text{seeds}} = 30$ wt.%) (b,d) aging, respectively, at two magnifications; Figure S3. X-ray diffractograms of two aged precursors from an unseeded ($x_{\text{seeds}} = 0$ wt.%) (a) and a seeded ($x_{\text{seeds}} = 30$ wt.%) (b) aging, showing the measured diffractogram in black and the phases determined by Rietveld refinement in color; Figure S4. X-ray diffractograms of two calcined precatalysts from an unseeded ($x_{\text{seeds}} = 0$ wt.%) (a) and a seeded ($x_{\text{seeds}} = 30$ wt.%) (b) aging, showing the measured diffractogram in black and the phases determined by Rietveld refinement in color; Figure S5. TEM-EDXS images of the calcined precatalysts for (a) the unseeded preparation at $t_{\text{age}} = 122$ min, (b) the unseeded preparation with a shortened aging step ($t_{\text{age}} = 60$ min) and (c) a seeded preparation ($x_{\text{seeds}} = 30$ wt.%) with a shortened aging step ($t_{\text{age}} = 55$ min). Cu is marked in red and Zr is marked in blue. The Zn distribution is shown in Figure 9; Figure S6. H₂-TPR profiles of the chosen precatalysts. References [31,34,41,65,83,84] are cited in Supplementary Materials.

Author Contributions: Conceptualization, D.G., S.P. and M.K.; methodology, D.G. and M.H.; validation, D.G., L.W., K.A. and M.H.; formal analysis, L.W. and K.A.; investigation, D.G., L.W., K.A., T.A.Z. and M.H.; resources, S.P. and M.K.; data curation, D.G., L.W. and M.H.; writing—original draft preparation, D.G.; writing—review and editing, D.G., L.W., M.H., T.A.Z., K.A., S.P. and M.K.; visualization, D.G.; supervision, S.P. and M.K.; project administration, D.G., S.P. and M.K. All authors have read and agreed to the published version of the manuscript.

Funding: Open access funding enabled and organized by Projekt DEAL.

Data Availability Statement: Data are contained within the article and Supplementary Materials.

Acknowledgments: The authors thank their students and colleagues at IKFT and TVT, especially Diana Deutsch, Thomas Otto and Abraham Karel, for their work in the lab and workshop. They kindly acknowledge the Laboratory for Electron Microscopy at the Karlsruhe Institute of Technology for conducting TEM(-EDXS) and SEM measurements.

Conflicts of Interest: The authors declare no conflicts of interest.

References

1. Gielen, D.; Dolan, G. *Innovation Outlook: Renewable Methanol*; Irena and Methanol Institute, Ed.; International Renewable Energy Agency: Abu Dhabi, United Arab Emirates, 2021; ISBN 978-92-9260-320-5.
2. Production of Methanol Worldwide from 2017 to 2022. Available online: <https://www.statista.com/statistics/1323406/methanol-production-worldwide/> (accessed on 20 March 2024).
3. Li, D.; Xu, F.; Tang, X.; Dai, S.; Pu, T.; Liu, X.; Tian, P.; Xuan, F.; Xu, Z.; Wachs, I.; et al. Induced activation of the commercial Cu/ZnO/Al₂O₃ catalyst for the steam reforming of methanol. *Nat. Catal.* **2022**, *5*, 99–108. [[CrossRef](#)]
4. Olah, G.A. Beyond Oil and Gas: The Methanol Economy. *Angew. Chem. Int. Ed.* **2005**, *44*, 2636–2639. [[CrossRef](#)]
5. Beck, A.; Newton, M.A.; van de Water, L.G.A.; van Bokhoven, J.A. The Enigma of Methanol Synthesis by Cu/ZnO/Al₂O₃-Based Catalysts. *Chem. Rev.* **2024**, *124*, 4543–4678. [[CrossRef](#)]
6. Pacchioni, G. From CO₂ to Methanol on Cu/ZnO/Al₂O₃ Industrial Catalyst. What Do We Know about the Active Phase and the Reaction Mechanism? *ACS Catal.* **2024**, *14*, 2730–2745. [[CrossRef](#)]
7. Arena, F.; Barbera, K.; Italiano, G.; Bonura, G.; Spadaro, L.; Frusteri, F. Synthesis, Characterization and Activity Pattern of Cu–ZnO/ZrO₂ Catalysts in the Hydrogenation of Carbon Dioxide to Methanol. *J. Catal.* **2007**, *249*, 185–194. [[CrossRef](#)]
8. Sternberg, A.; Bardow, A. Life Cycle Assessment of Power-to-Gas: Syngas vs. Methane. *ACS Sustain. Chem. Eng.* **2016**, *4*, 4156–4165. [[CrossRef](#)]
9. Bhardwaj, R.; Sharma, T.; Nguyen, D.D.; Cheng, C.K.; Lam, S.S.; Xia, C.; Nadda, A.K. Integrated Catalytic Insights into Methanol Production: Sustainable Framework for CO₂ Conversion. *J. Environ. Manag.* **2021**, *289*, 112468. [[CrossRef](#)]
10. Mondal, U.; Yadav, G.D. Methanol Economy and Net Zero Emissions: Critical Analysis of Catalytic Processes, Reactors and Technologies. *Green Chem.* **2021**, *23*, 8361–8405. [[CrossRef](#)]
11. Bampaou, M.; Haag, S.; Kyriakides, A.-S.; Panopoulos, K.D.; Seferlis, P. Optimizing Methanol Synthesis Combining Steelworks Off-Gases and Renewable Hydrogen. *Renew. Sustain. Energy Rev.* **2023**, *171*, 113035. [[CrossRef](#)]
12. Chinchin, G.C.; Denny, P.J.; Jennings, J.R.; Spencer, M.S.; Waugh, K.C. Synthesis of Methanol. Part 1. Catalysts and Kinetics. *Appl. Catal.* **1988**, *36*, 1–65. [[CrossRef](#)]
13. Bart, J.C.J.; Sneed, R.P.A. Copper-Zinc Oxide-Alumina Methanol Catalysts Revisited. *Catal. Today* **1987**, *2*, 1–124. [[CrossRef](#)]

14. Arena, F.; Italiano, G.; Barbera, K.; Bordiga, S.; Bonura, G.; Spadaro, L.; Frusteri, F. Solid-State Interactions, Adsorption Sites and Functionality of Cu-ZnO/ZrO₂ Catalysts in the CO₂ Hydrogenation to CH₃OH. *Appl. Catal. A Gen.* **2008**, *350*, 16–23. [[CrossRef](#)]
15. Wild, S.; Polierer, S.; Zevaco, T.A.; Guse, D.; Kind, M.; Pitter, S.; Herrera Delgado, K.; Sauer, J. Direct DME Synthesis on CZZ/H-FER from Variable CO₂/CO Syngas Feeds. *RSC Adv.* **2021**, *11*, 2556–2564. [[CrossRef](#)] [[PubMed](#)]
16. Słoczyński, J.; Grabowski, R.; Kozłowska, A.; Olszewski, P.; Lachowska, M.; Skrzypek, J.; Stoch, J. Effect of Mg and Mn Oxide Additions on Structural and Adsorptive Properties of Cu/ZnO/ZrO₂ Catalysts for the Methanol Synthesis from CO₂. *Appl. Catal. A Gen.* **2003**, *249*, 129–138. [[CrossRef](#)]
17. Köppel, R.A.; Stöcker, C.; Baiker, A. Copper- and Silver-Zirconia Aerogels: Preparation, Structural Properties and Catalytic Behavior in Methanol Synthesis from Carbon Dioxide. *J. Catal.* **1998**, *179*, 515–527. [[CrossRef](#)]
18. Peláez, R.; Bryce, E.; Marín, P.; Ordóñez, S. Catalyst Deactivation in the Direct Synthesis of Dimethyl Ether from Syngas over CuO/ZnO/Al₂O₃ and γ -Al₂O₃ Mechanical Mixtures. *Fuel Process. Technol.* **2018**, *179*, 378–386. [[CrossRef](#)]
19. Fichtl, M.B.; Schlereth, D.; Jacobsen, N.; Kasatkin, I.; Schumann, J.; Behrens, M.; Schlögl, R.; Hinrichsen, O. Kinetics of Deactivation on Cu/ZnO/Al₂O₃ Methanol Synthesis Catalysts. *Appl. Catal. A Gen.* **2015**, *502*, 262–270. [[CrossRef](#)]
20. Baltes, C.; Vukojevic, S.; Schuth, F. Correlations between Synthesis, Precursor, and Catalyst Structure and Activity of a Large Set of CuO/ZnO/Al₂O₃ Catalysts for Methanol Synthesis. *J. Catal.* **2008**, *258*, 334–344. [[CrossRef](#)]
21. Choi, Y.; Futagami, K.; Fujitani, T.; Nakamura, J. The Role of ZnO in Cu/ZnO Methanol Synthesis Catalysts—Morphology Effect or Active Site Model? *Appl. Catal. A Gen.* **2001**, *208*, 163–167. [[CrossRef](#)]
22. Fujitani, T.; Nakamura, J. The Chemical Modification Seen in the Cu/ZnO Methanol Synthesis Catalysts. *Appl. Catal. A Gen.* **2000**, *191*, 111–129. [[CrossRef](#)]
23. Liao, F.; Huang, Y.; Ge, J.; Zheng, W.; Tedsree, K.; Collier, P.; Hong, X.; Tsang, S.C. Morphology-Dependent Interactions of ZnO with Cu Nanoparticles at the Materials' Interface in Selective Hydrogenation of CO₂ to CH₃OH. *Angew. Chem. Int. Ed.* **2011**, *50*, 2162–2165. [[CrossRef](#)]
24. Palo, D.R.; Dagle, R.A.; Holladay, J.D. Methanol Steam Reforming for Hydrogen Production. *Chem. Rev.* **2007**, *107*, 3992–4021. [[CrossRef](#)]
25. Kuld, S.; Thorhauge, M.; Falsig, H.; Elkjær, C.F.; Helveg, S.; Chorkendorff, I.; Sehested, J. Quantifying the Promotion of Cu Catalysts by ZnO for Methanol Synthesis. *Science* **2016**, *352*, 969–974. [[CrossRef](#)]
26. Behrens, M.; Schlögl, R. How to Prepare a Good Cu/ZnO Catalyst or the Role of Solid State Chemistry for the Synthesis of Nanostructured Catalysts. *Z. Anorg. Allg. Chem.* **2013**, *639*, 2683–2695. [[CrossRef](#)]
27. Whittle, D.M.; Mirzaei, A.A.; Hargreaves, J.S.J.; Joyner, R.W.; Kiely, C.J.; Taylor, S.H.; Hutchings, G.J. Co-Precipitated Copper Zinc Oxide Catalysts for Ambient Temperature Carbon Monoxide Oxidation: Effect of Precipitate Ageing on Catalyst Activity. *Phys. Chem. Chem. Phys.* **2002**, *4*, 5915–5920. [[CrossRef](#)]
28. Spencer, M.S. The Role of Zinc Oxide in Cu/ZnO Catalysts for Methanol Synthesis and the Water–Gas Shift Reaction. *Top. Catal.* **1999**, *8*, 259–266. [[CrossRef](#)]
29. Behrens, M.; Girgsdies, F. Structural Effects of Cu/Zn Substitution in the Malachite-Rosasite System. *Z. Anorg. Allg. Chem.* **2010**, *636*, 919–927. [[CrossRef](#)]
30. Zwiener, L.; Girgsdies, F.; Brennecke, D.; Teschner, D.; Machoke, A.G.F.; Schlögl, R.; Frei, E. Evolution of Zincian Malachite Synthesis by Low Temperature Co-Precipitation and Its Catalytic Impact on the Methanol Synthesis. *Appl. Catal. B Environ.* **2019**, *249*, 218–226. [[CrossRef](#)]
31. Behrens, M.; Girgsdies, F.; Trunschke, A.; Schlögl, R. Minerals as Model Compounds for Cu/ZnO Catalyst Precursors: Structural and Thermal Properties and IR Spectra of Mineral and Synthetic (Zincian) Malachite, Rosasite and Aurichalcite and a Catalyst Precursor Mixture. *Eur. J. Inorg. Chem.* **2009**, *2009*, 1347–1357. [[CrossRef](#)]
32. Perchiazzi, N. Crystal Structure Determination and Rietveld Refinement of Rosasite and Mcguinnessite. In Proceedings of the Ninth European Powder Diffraction Conference, Prague, Czech Republic, 2–5 September 2004; Volume 23, pp. 505–510. [[CrossRef](#)]
33. Pollard, A.M.; Thomas, R.G.; Williams, P.A.; Just, J.; Bridge, P.J. The Synthesis and Composition of Georgeite and Its Reactions to Form Other Secondary Copper(II) Carbonates. *Mineral. Mag.* **1991**, *55*, 163–166. [[CrossRef](#)]
34. Pollard, A.M.; Spencer, M.S.; Thomas, R.G.; Williams, P.A.; Holt, J.; Jennings, J.R. Georgeite and Azurite as Precursors in the Preparation of Co-Precipitated Copper/Zinc Oxide Catalysts. *Appl. Catal. A Gen.* **1992**, *85*, 1–11. [[CrossRef](#)]
35. Guse, D.; Polierer, S.; Wild, S.; Pitter, S.; Kind, M. Improved Preparation of Cu/Zn-Based Catalysts by Well-Defined Conditions of Co-Precipitation and Aging. *Chem. Ing. Tech.* **2022**, *94*, 314–327. [[CrossRef](#)]
36. Bems, B.; Schur, M.; Dassenoy, A.; Junkes, H.; Herein, D.; Schlögl, R. Relations between Synthesis and Microstructural Properties of Copper/Zinc Hydroxycarbonates. *Chemistry* **2003**, *9*, 2039–2052. [[CrossRef](#)] [[PubMed](#)]
37. Mota, N.; Guil-Lopez, R.; Pawelec, B.G.; Fierro, J.L.G.; Navarro, R.M. Highly Active Cu/ZnO–Al Catalyst for Methanol Synthesis: Effect of Aging on Its Structure and Activity. *RSC Adv.* **2018**, *8*, 20619–20629. [[CrossRef](#)]
38. Angelo, L.; Girleanu, M.; Ersen, O.; Serra, C.; Parkhomenko, K.; Roger, A.-C. Catalyst Synthesis by Continuous Coprecipitation under Micro-Fluidic Conditions: Application to the Preparation of Catalysts for Methanol Synthesis from CO₂/H₂. *Catal. Today* **2016**, *270*, 59–67. [[CrossRef](#)]

39. Behrens, M.; Brennecke, D.; Girgsdies, F.; Kießner, S.; Trunschke, A.; Nasrudin, N.; Zakaria, S.; Idris, N.F.; Hamid, S.B.A.; Kniep, B.; et al. Understanding the Complexity of a Catalyst Synthesis: Co-Precipitation of Mixed Cu,Zn,Al Hydroxycarbonate Precursors for Cu/ZnO/Al₂O₃ Catalysts Investigated by Titration Experiments. *Appl. Catal. A Gen.* **2011**, *392*, 93–102. [[CrossRef](#)]
40. Frei, E.; Schaadt, A.; Ludwig, T.; Hillebrecht, H.; Krossing, I. The Influence of the Precipitation/Ageing Temperature on a Cu/ZnO/ZrO₂ Catalyst for Methanol Synthesis from H₂ and CO₂. *ChemCatChem* **2014**, *6*, 1721–1730. [[CrossRef](#)]
41. Zhang, Q.-C.; Cheng, K.-P.; Wen, L.-X.; Guo, K.; Chen, J.-F. A Study on the Precipitating and Aging Processes of CuO/ZnO/Al₂O₃ Catalysts Synthesized in Micro-Impinging Stream Reactors. *RSC Adv.* **2016**, *6*, 33611–33621. [[CrossRef](#)]
42. Kaluza, S.; Behrens, M.; Schiefenhövel, N.; Kniep, B.; Fischer, R.; Schlögl, R.; Muhler, M. A Novel Synthesis Route for Cu/ZnO/Al₂O₃ Catalysts Used in Methanol Synthesis: Combining Continuous Consecutive Precipitation with Continuous Aging of the Precipitate. *ChemCatChem* **2011**, *3*, 189–199. [[CrossRef](#)]
43. Polierer, S.; Guse, D.; Wild, S.; Herrera Delgado, K.; Otto, T.N.; Zevaco, T.A.; Kind, M.; Sauer, J.; Studt, F.; Pitter, S. Enhanced Direct Dimethyl Ether Synthesis from CO₂-Rich Syngas with Cu/ZnO/ZrO₂ Catalysts Prepared by Continuous Co-Precipitation. *Catalysts* **2020**, *10*, 816. [[CrossRef](#)]
44. Behrens, M. Meso- and Nano-Structuring of Industrial Cu/ZnO/(Al₂O₃) Catalysts. *J. Catal.* **2009**, *267*, 24–29. [[CrossRef](#)]
45. Schumann, J.; Lunkenbein, T.; Tarasov, A.; Thomas, N.; Schlögl, R.; Behrens, M. Synthesis and Characterisation of a Highly Active Cu/ZnO: Al Catalyst. *ChemCatChem* **2014**, *6*, 2889–2897. [[CrossRef](#)]
46. Guse, D.; Warmuth, L.; Kreißig, F.; Pitter, S.; Kind, M. Preparation of Cu/Zn Based Catalyst Precursors—Importance of Thermodynamics and Seeding. In Proceedings of the DGMK-Conference “The Role of Catalysis for the Energy Transition“, Ludwigshafen, Germany, 5–7 October 2022; Volume 2022–2023, pp. 19–39. [[CrossRef](#)]
47. Güldenpfennig, A.; Distaso, M.; Peukert, W. In Situ Investigations on the Amorphous to Crystalline Phase Transformation of Precursors for Methanol Synthesis Catalysts. *Chem. Eng. J.* **2019**, *369*, 996–1004. [[CrossRef](#)]
48. Zander, S.; Seidlhofer, B.; Behrens, M. In Situ EDXRD Study of the Chemistry of Aging of Co-Precipitated Mixed Cu,Zn Hydroxycarbonates—Consequences for the Preparation of Cu/ZnO Catalysts. *Dalton Trans.* **2012**, *41*, 13413–13422. [[CrossRef](#)] [[PubMed](#)]
49. Farahani, B.V.; Rajabi, F.H.; Bahmani, M.; Ghelichkhani, M.; Sahebdehfar, S. Influence of Precipitation Conditions on Precursor Particle Size Distribution and Activity of Cu/ZnO Methanol Synthesis Catalyst. *Appl. Catal. Gen.* **2014**, *482*, 237–244. [[CrossRef](#)]
50. Muhamad, E.N.; Irmawati, R.; Taufiq-Yap, Y.H.; Abdullah, A.H.; Kniep, B.L.; Girgsdies, F.; Ressler, T. Comparative Study of Cu/ZnO Catalysts Derived from Different Precursors as a Function of Aging. *Catal. Today* **2008**, *131*, 118–124. [[CrossRef](#)]
51. Smith, P.J.; Kondrat, S.A.; Chater, P.A.; Yeo, B.R.; Shaw, G.M.; Lu, L.; Bartley, J.K.; Taylor, S.H.; Spencer, M.S.; Kiely, C.J.; et al. A New Class of Cu/ZnO Catalysts Derived from Zincian Georgeite Precursors Prepared by Co-Precipitation. *Chem. Sci.* **2017**, *8*, 2436–2447. [[CrossRef](#)]
52. Sengupta, G.; Das, D.P.; Kundu, M.L.; Dutta, S.; Roy, S.K.; Sahay, R.N.; Mishra, K.K.; Ketchik, S.V. Study of Copper—Zinc Oxide Catalysts, Characterisation of the Coprecipitate and Mixed Oxide. *Appl. Catal.* **1989**, *55*, 165–180. [[CrossRef](#)]
53. Kaluza, S.; Muhler, M. On the Role of Aging, Washing, and Drying in the Synthesis of Polycrystalline Zinc Oxide by Precipitation: Combining Fast Continuous Mixing, Spray Drying and Freeze Drying to Unravel the Solid-State Transformations of the Precipitate. *Catal. Lett.* **2009**, *129*, 287–292. [[CrossRef](#)]
54. Schumann, J.; Tarasov, A.; Thomas, N.; Schlögl, R.; Behrens, M. Cu,Zn-Based Catalysts for Methanol Synthesis: On the Effect of Calcination Conditions and the Part of Residual Carbonates. *Appl. Catal. A Gen.* **2016**, *516*, 117–126. [[CrossRef](#)]
55. Mullin, J.W. *Crystallization*, 4th ed.; Butterworth-Heinemann: Oxford, UK, 2001; ISBN 978-0-7506-4833-2.
56. Manuel García-Ruiz, J. Nucleation of Protein Crystals. *J. Struct. Biol.* **2003**, *142*, 22–31. [[CrossRef](#)] [[PubMed](#)]
57. Myerson, A.S. *Handbook of Industrial Crystallization*, 2nd ed.; Butterworth-Heinemann: Boston, UK, 2002; ISBN 978-0-08-053351-3.
58. Beckmann, W. *Crystallization: Basic. Concepts and Industrial Applications*; John Wiley & Sons: Hoboken, NJ, USA, 2013; ISBN 1-299-15731-9.
59. Threlfall, T.L.; De’Ath, R.W.; Coles, S.J. Metastable Zone Widths, Conformational Multiplicity, and Seeding. *Org. Process Res. Dev.* **2013**, *17*, 578–584. [[CrossRef](#)]
60. Threlfall, T.L.; Coles, S.J. A Perspective on the Growth-Only Zone, the Secondary Nucleation Threshold and Crystal Size Distribution in Solution Crystallisation. *CrystEngComm* **2016**, *18*, 369–378. [[CrossRef](#)]
61. Barros Groß, M.; Kind, M. Comparative Study on Seeded and Unseeded Bulk Evaporative Batch Crystallization of Tetragonal Lysozyme. *Cryst. Growth Des.* **2017**, *17*, 3491–3501. [[CrossRef](#)]
62. Jiang, X.; Zheng, L.; Wang, Z.; Lu, J. Microstructure Characters of Cu/ZnO Catalyst Precipitated inside Microchannel Reactor. *J. Mol. Catal. A Chem.* **2016**, *423*, 457–462. [[CrossRef](#)]
63. Jiang, X.; Qin, X.; Ling, C.; Wang, Z.; Lu, J. The Effect of Mixing on Co-Precipitation and Evolution of Microstructure of Cu-ZnO Catalyst. *AIChE J.* **2018**, *124*, 123. [[CrossRef](#)]
64. Klokishner, S.; Behrens, M.; Reu, O.; Tzolova-Müller, G.; Girgsdies, F.; Trunschke, A.; Schlögl, R. Cation Ordering in Natural and Synthetic (Cu_{1-x}Zn_x)₂CO₃(OH)₂ and (Cu_{1-x}Zn_x)₅(CO₃)₂(OH)₆. *J. Phys. Chem. A* **2011**, *115*, 9954–9968. [[CrossRef](#)]
65. Kondrat, S.A.; Smith, P.J.; Wells, P.P.; Chater, P.A.; Carter, J.H.; Morgan, D.J.; Fiordaliso, E.M.; Wagner, J.B.; Davies, T.E.; Lu, L.; et al. Stable Amorphous Georgeite as a Precursor to a High-Activity Catalyst. *Nature* **2016**, *531*, 83–87. [[CrossRef](#)] [[PubMed](#)]
66. Loï Mi Lung-Somarrriba, B.; Moscossa-Santillan, M.; Porte, C.; Delacroix, A. Effect of Seeded Surface Area on Crystal Size Distribution in Glycine Batch Cooling Crystallization: A Seeding Methodology. *J. Cryst. Growth* **2004**, *270*, 624–632. [[CrossRef](#)]

67. Choi, J.Y.; Lee, T.; Cheng, Y.; Cohen, Y. Observed Crystallization Induction Time in Seeded Gypsum Crystallization. *Ind. Eng. Chem. Res.* **2019**, *58*, 23359–23365. [CrossRef]
68. Evans, T.W.; Sarofim, A.F.; Margolis, G. Models of Secondary Nucleation Attributable to Crystal-Crystallizer and Crystal-Crystal Collisions. *AIChE J.* **1974**, *20*, 959–966. [CrossRef]
69. Kaysan, G.; Rica, A.; Guthausen, G.; Kind, M. Contact-Mediated Nucleation of Subcooled Droplets in Melt Emulsions: A Microfluidic Approach. *Crystals* **2021**, *11*, 1471. [CrossRef]
70. Zhang, K.; Chanpura, R.A.; Mondal, S.; Wu, C.-H.; Sharma, M.M.; Ayoub, J.A.; Parlar, M. Particle Size Distribution Measurement Techniques and Their Relevance or Irrelevance to Sand Control Design. In Proceedings of the SPE International Conference and Exhibition on Formation Damage Control, Lafayette, LA, USA, 26 February 2014.
71. D’Ans, J.; Lax, E. *Taschenbuch Für Chemiker Und Physiker.: Band I: Makroskopische Physikalisch-Chemische Eigenschaften*, 3rd ed.; Springer: Berlin/Heidelberg, Germany; New York, NY, USA, 1967.
72. Waller, D.; Stirling, D.; Stone, F.S.; Spencer, M.S. Copper–Zinc Oxide Catalysts. Activity in Relation to Precursor Structure and Morphology. *Faraday Discuss. Chem. Soc.* **1989**, *87*, 107–120. [CrossRef]
73. Kniep, B.L.; Girgsdies, F.; Ressler, T. Effect of Precipitate Aging on the Microstructural Characteristics of Cu/ZnO Catalysts for Methanol Steam Reforming. *J. Catal.* **2005**, *236*, 34–44. [CrossRef]
74. Frusteri, F.; Cordaro, M.; Cannilla, C.; Bonura, G. Multifunctionality of Cu–ZnO–ZrO₂/H-ZSM5 Catalysts for the One-Step CO₂-to-DME Hydrogenation Reaction. *Appl. Catal. B Environ.* **2015**, *162*, 57–65. [CrossRef]
75. Warmuth, L.; Steurer, M.; Schild, D.; Zimina, A.; Grunwaldt, J.-D.; Pitter, S. Reversible and Irreversible Structural Changes in Cu/ZnO/ZrO₂ Catalysts during Methanol Synthesis. *ACS Appl. Mater. Interfaces* **2024**, *16*, 8813–8821. [CrossRef] [PubMed]
76. Stangeland, K.; Li, H.; Yu, Z. Thermodynamic Analysis of Chemical and Phase Equilibria in CO₂ Hydrogenation to Methanol, Dimethyl Ether, and Higher Alcohols. *Ind. Eng. Chem. Res.* **2018**, *57*, 4081–4094. [CrossRef]
77. Doebelin, N.; Kleeberg, R. Profex: A Graphical User Interface for the Rietveld Refinement Program BGMN. *J. Appl. Crystallogr.* **2015**, *48*, 1573–1580. [CrossRef]
78. Malvern Instruments Ltd. *Zetasizer Nano User Manual*; Malvern Instruments Ltd.: Malvern, UK, 2013.
79. Mastersizer User Guide 2024. Available online: <https://www.malvernpanalytical.com/de/learn/knowledge-center/user-manuals/man0474en> (accessed on 12 June 2024).
80. Malvern Panalytical. Malvern Panalytical Selecting an Appropriate Particle Absorption for Laser Diffraction Particle Size Calculations. Available online: <https://www.malvernpanalytical.com/en/learn/knowledge-center/technical-notes/TN101104SelectingParticleAbsorbtionLaserDiffractio> (accessed on 12 June 2024).
81. Wild, S.; Lacerda de Oliveira Campos, B.; Zevaco, T.A.; Guse, D.; Kind, M.; Pitter, S.; Herrera Delgado, K.; Sauer, J. Experimental Investigations and Model-Based Optimization of CZZ/H-FER 20 Bed Composition for the Direct Synthesis of DME from CO₂-Rich Syngas. *React. Chem. Eng.* **2022**, *7*, 943–956. [CrossRef]
82. Judat, B.; Kind, M. Morphology and Internal Structure of Barium Sulfate—Derivation of a New Growth Mechanism. *J. Colloid. Interface Sci.* **2004**, *269*, 341–353. [CrossRef]
83. Shen, G.-C.; Fujita, S.; Matsumoto, S.; Takezawa, N. Steam Reforming of Methanol on Binary CuZnO Catalysts: Effects of Preparation Condition upon Precursors, Surface Structure and Catalytic Activity. *J. Mol. Catal. A Chem.* **1997**, *124*, 123–136. [CrossRef]
84. Fujita, S.; Satriyo, A.M.; Shen, G.C.; Takezawa, N. Mechanism of the Formation of Precursors for the Cu/ZnO Methanol Synthesis Catalysts by a Coprecipitation Method. *Catal. Lett.* **1995**, *34*, 85–92. [CrossRef]

Disclaimer/Publisher’s Note: The statements, opinions and data contained in all publications are solely those of the individual author(s) and contributor(s) and not of MDPI and/or the editor(s). MDPI and/or the editor(s) disclaim responsibility for any injury to people or property resulting from any ideas, methods, instructions or products referred to in the content.